GEOCHEMISTRY AND GROWTH MORPHOLOGY OF ALKALI FELDSPAR CRYSTALS FROM AN IAB IRON METEORITE – INSIGHT INTO POSSIBLE HYPOTHESES OF THEIR CRYSTALLIZATION

Ewa SŁABY[1], Łukasz KARWOWSKI[2], Katarzyna MAJZNER[3, 4], Richard WIRTH[5], Andrzej MUSZYŃSKI[6], Łukasz BIRSKI[1], Klaus SIMON[7], Andrzej DOMONIK[8], Izabela MOSZUMAŃSKA[1] & Ryszard ORŁOWSKI[1]

[1] *Institute of Geological Sciences, Polish Academy of Sciences, Research Centre in Warsaw, Twarda 51/55, 00-818 Warszawa, Poland; e-mails: e.slaby@twarda.pan.pl, l.birski@twarda.pan.pl, i.moszumanska@twarda.pan.pl, rorlowsk@twarda.pan.pl*

[2] *Faculty of Earth Sciences, University of Silesia, Będzińska 60, 41-200 Sosnowiec, Poland; e-mail: lukasz.karwowski@us.edu.pl*

[3] *Faculty of Chemistry, Jagiellonian University, Gronostajowa 2, 30-387 Kraków, Poland; e-mail: majzner@chemia.uj.edu.pl*

[4] *Jagiellonian Centre for Experimental Therapeutics (JCET), Jagiellonian University, Bobrzyńskiego 14, 30-348 Kraków, Poland*

[5] *Helmholtz-Zentrum Potsdam Deutsches GeoForschungsZentrum GFZ, Telegrafenberg, 14473 Potsdam, Germany GHZ; e-mail: wirth@gfz-potsdam.de*

[6] *Institute of Geology, Adam Mickiewicz University, Maków Polnych 16, 61-606 Poznań, Poland; e-mail: anmu@amu.edu.pl*

[7] *Department of Geochemistry, GZG of Georg-August-University, Goldschmidtstrasse 1, 37077 Göettingen, Germany; e-mail: ksimon@gwdg.de*

[8] *Institute of Hydrogeology and Engineering Geology, University of Warsaw, 02-089 Warszawa, Żwirki i Wigury 93, Poland; e-mail: adomonik@uw.edu.pl*

Abstract: Alkali feldspar crystals have been recognized in the troilite-graphite nodules of the Morasko IAB iron meteorite. Their chemical, microtextural and structural properties were studied using electron microprobe analysis (EMPA), laser ablation inductively coupled plasma mass spectrometry (LA-ICP-MS), transmission electron microscopy (TEM) and Raman spectroscopy. The feldspars occur as perthitic or antiperthitic intergrowths, whereas the albite lamellae are perfectly twinned. The structural properties reveal intergrown phases with fairly disordered patterns. The electron microprobe analyses demonstrate that the intergrown phases are mainly rich in sodium or potassium, resulting in compositions that are close to those of albite or orthoclase. The compositions, calculated on the basis of a segmented perthite-antiperthite image, showed that the Or-to-Ab proportions in the homogenized crystals were almost 0.3:0.7, thus indicating that the anorthoclase crystallized under high-temperature conditions. Two hypotheses of crystal formation could account for these characteristics: crystallization from a melt or from a metasomatic solution. Relics with evidence of metasomatic replacement of former minerals were not found. Accordingly, this work focuses on arguments that support the other hypothesis. Large ion lithophile elements (LILEs, e.g., Ba, Sr, Rb, LREE, Pb, and Ga) were used to track the origin of the crystals. Their concentrations indicate crystallization from a parent melt strongly depleted in LILEs. Alkali feldspar is commonly a product of a highly differentiated melt. However, highly differentiated melts are typically enriched in LILEs, which here is not the case. The melt that crystallized the feldspar cannot be related to impact-induced partial melting of the chondritic material alone. The derived melt probably was contaminated by silica-rich target material during interaction between the IAB projectile and the target material and was accompanied by metal and sulphide melts that were both immiscible with a silicate melt.

Key words: IAB, iron meteorite, alkali feldspar, trace elements, growth texture, perthite/antiperthite, melt contamination, target material.

INTRODUCTION

The IAB meteorites are a group of iron meteorites composed of meteoritic iron (kamacite and taenite). They contain silicate inclusions, the composition of which shows an affinity to primitive achondrites. The textural and compositional properties of iron and silicates in IAB meteorites are explained by numerous processes. Different mechanisms may control the degree of partial melting, the melt segregation, migration and evolution (Goldstein *et al.*, 2009 and references therein). Choi *et al.* (1995) and Mittlefehldt *et al.* (1998) reviewed some general ideas on models of IAB formation. They discussed two possible processes: 1) partial melting and segregation of the melt into numerous pools rather than a single core, and 2) impact melting and segregation of metal from chondritic material into numerous pools. Wasson *et al.* (1980) and Choi *et al.* (1995) suggested that variations in the degree of impact melting alone could lead to the main compositional differences observed in IAB objects.

One important question concerns heat-source-induced melting. The Wasson and Kallemeyn (2002) model indicated that the metallic melt was produced mainly by impact heating, whereas the other models indicate that internal heat sources such as the decay of ^{26}Al account for the melting process (Kracher, 1985; Takeda *et al.*, 1985; McCoy *et al.*, 1993; Benedix *et al.*, 2000). The formation of metallic pools may result from the impact melting of cold chondritic material (Choi *et al.*, 1995; Wasson and Kallemeyn, 2002) or from the impact fragmentation of an already hot and partially molten body (Benedix *et al.*, 2000, 2005). The formation of silicate inclusions in IAB meteorites is explained in the Wasson and Kallemeyn (2002) model by selective impact melting of chondritic material and its subsequent crystallization under conditions of rapid heating and cooling. They argued that IAB formation involves crystal segregation in which the solids and melts are basically in equilibrium. Multiple impact-generated melting events created the different subgroups. They excluded fractional crystallization as a mechanism causing efficient melt evolution. Crystal segregation allows rapid metal fractionation and causes viscosity change, keeping silicates in suspension. Benedix *et al.* (2000) suggested incomplete partial melting and the separation of metal, FeS and mafic melts, followed by an impact-generated silica-metal mix. In their model, they proposed the possibility of five lithologies produced by impacts that were followed by mixing with metallic molten portions. In contrast to the Wasson and Kallemeyn (2002) model, they considered fractional crystallization as a mechanism that triggers metal fractionation. As a result, they supposed that clear fractional crystallization trends accompany the distribution of metals within the IAB body.

Takeda *et al.* (2000) studied the growth textures and phase composition of melted chondritic material such as gabbroidal products (sodium-rich plagioclase and diopside) from the crystallization of mafic melt segregated from an ultramafic residue. Takeda *et al.* (2000) reviewed interpretations of the origin and relationship between IAB and primitive achondrites. To primitive achondrites belong acapulcoites, winonaites and lodranites. Acapulcoites are chon-

dritic in composition. If partial melting occurs in them, the melt is not separated from the residue (Mittlefehldt *et al.*, 1996). Similarly, winonaites are products of partial melting and recrystallization of chondritic material. Lodranites are ultramafic residues left behind after partial melting.

The processes described above are mostly related to melting and crystallization. They generate plagioclase, but the emergence of alkali feldspar is reported very rarely. Plagioclase associated with alkali feldspar was studied by Bunch and Olsen (1968) and Wassenburg *et al.* (1968) in the Kodaikanal and Colomera iron meteorites. They presented the feldspar composition, but did not discuss the mechanisms of its formation. In turn, alkali feldspar associated with plagioclase of secondary or primary origin has been found in numerous chondrites (Kovach and Jones, 2010; Gallegos and Jones, 2011; Jones and Brearley, 2011; Lewis and Jones, 2015, 2016; Lewis *et al.*, 2016). The origin of the alkali feldspar is explained as resulting from alkali metasomatism.

The IAB Morasko meteorite contains troilite-graphite oval nodules with some generations of silicates. The diversity of the silicate association in individual nodules may indicate both numerous melting and crystallization processes influencing their formation and maybe separation of these processes in time. Successive silicate generations and their relationship to the ultramafic residue left after partial melting and to melt evolution are the subject of this contribution. Partial melting of chondrites leads to the appearance of a mafic melt. However, the mafic component is missing. Instead of plagioclase, the nodules contain alkali feldspar. This study is the first to describe the trace-element characteristics of the feldspar and to present Raman images of the feldspar crystals and their surrounding domains. The geochemistry and growth morphology of the alkali feldspar crystals may indicate alkali metasomatism as a process responsible for their formation. However, multi-stage impact-induced partial melting followed by mixing of the melts may also explain their formation. On the basis of the data collected, the authors discuss both hypotheses.

BACKGROUND TO SAMPLE SELECTION

The Morasko meteorite, found in 1914 in an area north of Poznań (central-west Poland; Stankowski, 2008; Pilski *et al.*, 2013 and references therein), is classified as an IAB-MG octahedrite. Its mineral composition has been the subject of many studies (Dominik, 1976; Dziel *et al.*, 2007; Karwowski and Muszyński, 2008; Muszyński *et al.*, 2012; Pilski *et al.*, 2013; Karwowski *et al.*, 2015). The predominant matrix of iron (kamacite and taenite) contains troilite-graphite oval nodules (Fig. 1A) that are commonly rimmed by cohenite and a small quantity of an admixture of schreibersite and djerfisherite, usually adjoining troilite and graphite. Occasionally sphalerite and altaite occur in the rim (Muszyński *et al.*, 2001, 2012). The nodules are up to several cm in diameter. In addition to the troilite-graphite, the nodules contain several silicate minerals, including pyroxenes (enstatite, kosmochlor-augite solid solution and kosmochlor), olivines, alkali feldspars (Fig. 1B), and quartz
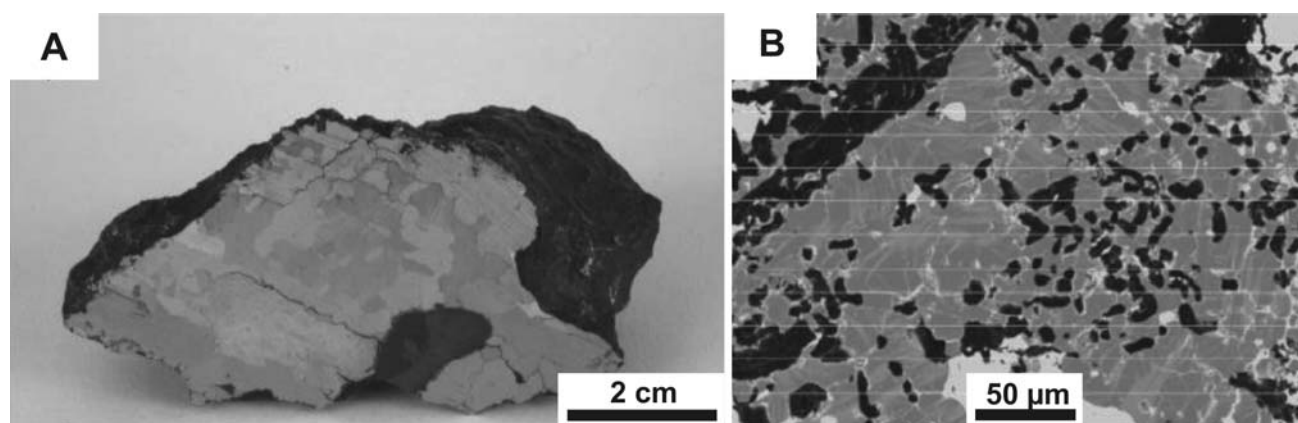
Fig. 1. Silicate nodule in Morasko IAB-MG octahedrite. **A.** Kamacite and taenite matrix with dark-grey nodule. **B.** BSE image of alkali feldspar with troilite (white) and graphite (black) in the nodule.

(Karwowski and Muszyński, 2006; Karwowski *et al.*, 2012). The troilite in the nodules is associated with daubreelite and pyrrothite. Many other accessory phases have been reported from the nodules. These include chromite, sphalerite, whitlockite (Dominik, 1976), altaite, rutile, native copper (Muszyński *et al.*, 2001; Karwowski *et al.*, 2012), and numerous phosphates (moraskoite, buchwaldite, brianite, merrillite, apatite and others; Karwowski *et al.*, 2009, 2015). Various alteration products, such as Ni-bearing iron hydroxides, chlorites, sulphates, phosphates and carbonates, accompany the primary poly-phase association (Karwowski and Gurdziel, 2009).

METHODS

Electron Microprobe Analysis (EMPA)

Analyses of the alkali feldspar crystals were performed with a Cameca SX-100 (accelerating voltage of 15 kV; two beam-current conditions) at the Faculty of Geology, University of Warsaw (Inter-Institute Analytical Complex for Minerals and Synthetic Substances). The Na, K, Ca, Si and Al were analyzed at 15 nA, and Ba, Mg, Sr and Fe were analyzed at 50 nA. The counting times were 30 s for Ba and Sr, 60 s for Fe and Mg, and 10 s for Al, Si, and Ca. The representative detection limits (3σ) for minor and trace elements were 220 ppm for Ba, 400 ppm for Sr, 200 ppm for Fe and 40 ppm for Mg. The following P&H Developments standards were used: albite, diopside, orthoclase, and barite. Thin-section elemental maps were collected to identify phase relationships in the thin sections. Analytical conditions were as follows: 20 kV accelerating voltage, 100 nA beam current, 10 μm steps; 2100 cps/s, 2,700 sweep counts, and an analysis time of 17 h.

Laser Ablation Inductively Coupled Plasma Mass Spectrometry (LA-ICP-MS)

LA-ICP-MS analyses were performed using a FISONS VG PQ STE instrument with a VG UV Microprobe laser system (266 nm) at the Geochemisches Institut, Göttingen Uni-

versity. The feldspar crystals, pyroxene, taenite and kamacite were analyzed for ^{23}Na, ^{24}Mg, ^{27}Al, ^{29}Si, ^{31}P, ^{34}S, ^{35}Cl, ^{39}K, ^{43}Ca, ^{45}Sc, ^{49}Ti, ^{51}V, ^{53}Cr, ^{55}Mn, ^{57}Fe, ^{59}Co, ^{60}Ni, ^{63}Cu, ^{66}Zn, ^{71}Ga, ^{73}Ge, ^{75}As, ^{77}Se, ^{85}Rb, ^{88}Sr, ^{93}Nb, ^{111}Cd, n ^{118}Sn, ^{121}Sb, ^{137}Ba, ^{139}La, ^{140}Ce, ^{195}Pt, ^{197}Au, ^{205}Tl, ^{206}Pb, ^{208}Pb and ^{209}Bi, ^{232}Th. The elemental concentrations were calculated using NBS610 for calibration and ^{29}Si as an internal standard. The major element oxides were normalized to 100%. The operating conditions are given in Table 1

Table 1

Laser Ablation ICP-MS analysis – operating conditions and data acquisition parameters

ICP-MS	
Model	PerkinElmer DRC II
Forward power	1250 W
Gas flows	
Coolant (plasma) Ar	14 l min^{-1}
Auxiliary Ar	0.95 l min^{-1}
Transport Ar	ca 1.2 l min^{-1}
Laser	
Model	Lambda Physik Compex 110 with GeoLas optical bank from MikroLas
Wavelength	193 nm
Pulse width (FWHM)	20 ns
Pulse energy	160 mJ/pulse
Energy distribution	Homogenized, flat beam, aperture imaged
Energy density	25 J cm^{-2} on sample surface
Focus	Fixed at surface
Repetition rate	10 Hz
Crater diameter	Approx. 60 μm
Analysis protocol	
Scanning mode	Peak jumping, 1 point/peak
Acquisition mode	Time resolved analysis, dwell time 20 ms for all isotopes, 0.943 s/sweep, 100 repeats
Analysis duration	Approx. 95 s integration

Raman imaging

Raman measurements were performed with a WITec alpha300 confocal Raman imaging system using a Nikon 20× air objective (SPlan Fluor Nikon, NA = 0.45). The WITec Raman spectrometer was equipped with a 600-groove/mm grating (BLZ=500 nm) with a spectral resolution of approximately 3 cm^{-1}, and the Nd:YAG dye laser has a maximum power at the source of approximately 40 mW power at 532 nm. Raman spectroscopic data resulting from imaging with the excitation wavelength of 532 nm and a laser power of approximately 20 mW at the sample were obtained by collecting spectra via 0.3–0.5 second exposure times and moving the sample in increments of 3 μm (165×165 μm^2, 3,025 points). The WITec Project Plus software enabled investigation of the spatial distribution of the phase components in the samples measured by integrating the selected bands and performing k-means cluster analysis. All spectra were baseline corrected using a polynomial of degree 3 or 6 and the routine procedure for cosmic-ray removal was applied.

K-means cluster analysis (KMC) was performed using a Manhattan algorithm as a distance measurement and a linkage method according to the City Block Algorithm (normalization of spectra to the 80–1700 cm^{-1} region using the Manhattan normalization mode; MacQueen, 1967). The mean spectra of the classes obtained were calculated by averaging the original spectra from all pixels within a class. The normalization, linear baseline correction, deconvolution, and integration of bands were all conducted using Bruker's OPUS7.0 software. The spectra were normalized to the 1190–1734 cm^{-1} spectral range using the vector normalization method and the integrated areas of selected bands were calculated.

Transmission Electron Microscope (TEM)

Sampling was performed *via* focused ion beam (FIB) milling. TEM-ready foils of approximately 20 × 10 × 0.15 μm were cut directly from the crystal grain in the epoxy grain mount. Once cut, the TEM foils were placed on a perforated carbon film atop a copper grid. The sample was coated with a thin layer of carbon to prevent charging in the TEM. TEM analysis was conducted using a Philips CM200 instrument with a beam current of 200 kV and a LaB6 electron source, at the GFZ in Potsdam. The electron energy-loss spectra (EELS) were acquired with a Gatan imaging filter (GIF).

Image segmentation

Wayne Rasband's program (Schneider *et al.*, 2012) was used for image processing and analysis. The image was transformed to a high-resolution TIFF (Tagged Image File Format) file. This file format uses lossless compression. The contrast and brightness were levelled relative to the central part of the area near the edge of the photo. During segmentation, the fields were isolated using a thresholding tool and grey values on a scale of 0 to 255, which corresponded to the shades of grey of the analyzed fields. The isolated individual fields were converted into binary images. The last step was a filtering process to remove structural artifacts. Phase analyses were performed on the binary images representing each field. The number of pixels that made up each individual field was counted.

RESULTS

Feldspar growth morphology– relationship to other phases

The nodule BSE image (Fig. 2) shows a complicated mosaic of minerals, which seem to have crystallized at different stages of nodule formation. An assemblage of troilite, graphite (Fig. 2; Tr-Gr) and silicate (Fig. 2; Fs, Px) with diverse shapes is interconnected by veins of Fe-Ni oxide-hydroxide (Fig. 2; Fe-Ni ox-hy). Feldspar crystals are enclosed in the troilite-graphite mixture or pyroxene, and their distribution is very irregular. On the low-magnification BSE image (Figs 2, 3A, B), they present apparently homogeneous, rounded areas with a size of up to 0.2 mm. Under higher magnification (Figs 1B, 3C, D), the feldspar appears in the form of irregular clusters of variably oriented crystals. The clusters contain graphite and troilite. They are seldom included in feldspar crystals as inclusions and mostly appear at the borders between crystals.

Also at a higher magnification, the seemingly homogeneous feldspar crystals exhibit perthitic/antiperthitic patterns. The exsolved lamellae have irregular shapes. Frequently, they do not have similar widths and do not continue through the whole crystal. It appears that in each crystal the exsolution process proceeds at a different rate (Figs 1B, 3C, D). The albite-rich lamellae in the intergrown phases are perfectly twinned (Fig. 4). Feldspar is primarily associated with pyroxene. Kosmochlor and Cr-rich Na-Ca pyroxenes in kosmochlor-augite solid-solution form rims on Mg-rich pyroxenes (Karwowski and Muszyński, 2006). In some places, alkali feldspar occurs with enstatite, but without kosmochlor.

Mineral chemistry

Electron Microprobe Analysis

The chemical compositions of the Ab-Or intergrowths (perthite/antiperthite) are shown in Table 2 and Figure 4. The data indicate that even if all the exsolution occurrences in crystals from the clusters contain the three end-members of the ternary solid-solution, the composition of the intergrowths is rich in either potassium or sodium. In the albite-rich lamellae in the intergrown phases, the orthoclase and anorthite end-members are very low, ranging from 1.03–6.15 and 0.00–2.59, respectively. Similarly, in K-rich lamellae in the intergrown phases, albite and anorthite end-members are also low, ranging from 0.00–18.98 and 0.00–0.39, respectively.

The intergrowths in five crystals from the cluster shown in Fig. 3D were first analyzed for recalculation of the homogeneous crystal composition. Subsequently, the image of these crystals was graphically decomposed into five segments (Fig. 5). The analyzed areas of albite (dark grey) and orthoclase (black) yield the approximate proportions
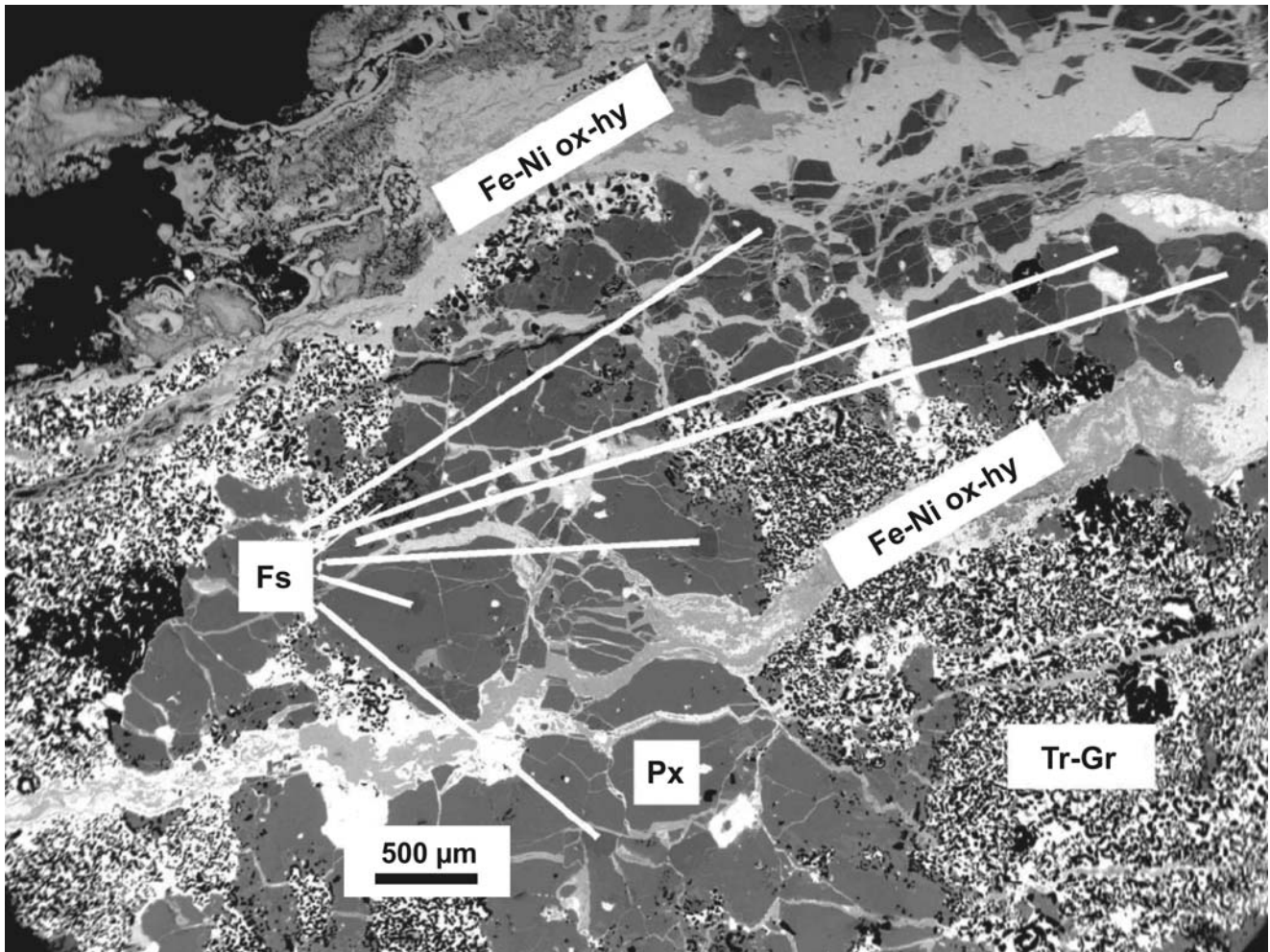
Fig. 2.   Phase relationship in the nodule, BSE – back-scattered electron image. Abbreviations: Fs – feldspar, Px – pyroxene, Fe-Ni ox-hy - Fe-Ni oxide-hydroxide, Tr-Gr – troilite-graphite matrix.

Ab_{72}:Or_{28} (the light grey hexagon in Fig. 4). A number of the fields can be marked as fields with a high degree of uncertainty regarding their composition. In Fig. 5, they are visible in the form of order-independent intergrowths, oriented in many different directions. These areas of uncertainty are marked with a light-grey color. Assigning light grey areas to more Or-rich compositions, the proportions between Or-Ab particles change in favor of the more potassium-rich and oscillate around the composition Or_{56}:Ab_{44} (dark grey hexagon in Fig. 4). However, in assigning them to an Ab-rich composition, the proportions between the Or-Ab particles change in favour of greater sodium content. Because this calculation covered the areas of high uncertainty, the most probable value of the composition of the feldspar before admixing is close to the outcome obtained for the antiperthite pattern within single grains, e.g., ~Ab_{70}:Or_{30}. The procedure was repeated for the next crystals (five crystals with well-developed exsolution patterns) from other areas of the cluster (Fig. 3C). These procedures yielded similar results, e.g. a composition close to Ab_{70}:Or_{30}. Apart from the perthitic/antiperthitic crystals, single crystals (up to 10 µm) of potassium feldspar have been found with a composition close to Or_{100}. They are homogeneous.

Feldspars contain inclusions of graphite and troilite. They are interconnected, framed or cut by veins of Fe-Ni oxide-hydroxide, which are also enriched in chlorine (Table 3). The veins reveal a multi-phase mixture of minute crystals (Fig. 2; Table 3). In some places, the mixture shows significant enrichment in Cr and in others, a variable sulphur concentration. Small areas within veins are pure Fe-Ni.

Laser Ablation-Inductively Coupled Plasma-Mass Spectrometry

Laser ablation ICP-MS analyses were performed on carefully chosen spots with no visible inclusions. The results are shown in Table 4. Only sodium-enriched feldspar crystals were large enough to permit an analysis within a crystal area. The K-rich feldspar were too small for analysis. Despite careful selection, none of the spots yielded compositions that could be attributed to pure feldspar. The spot labelled as 13 is very close to the composition of feldspar. It still has a high iron content, but such an iron content is also reported from EMPA measurements. A similar iron content was measured in alkali feldspar by Bunch and Olsen (1968) in the Kodaikanal and Colomera iron meteorites. In contrast, in spot 15, which seems also to be close to a Na-rich
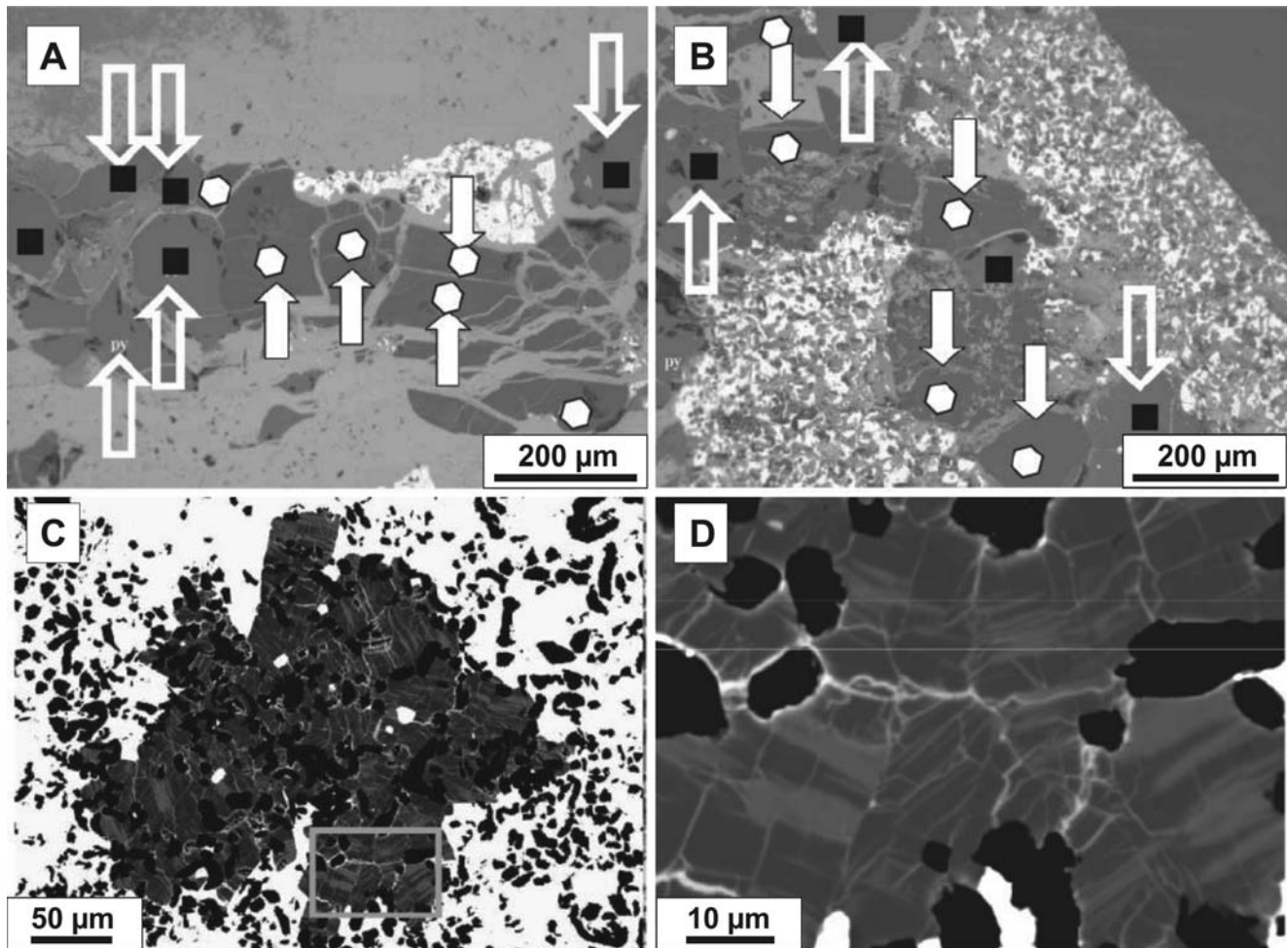
Fig. 3. BSE images of the feldspar growth morphology. **A.** Pyroxene (black rectangle) – feldspar (white hexagon) phase relationship (light grey area – Fe-Ni oxide-hydroxide, white spot – troilite). **B.** Feldspar and pyroxene in the troilite-graphite-Fe oxide-hydroxide matrix. **C.** Feldspar crystal mosaic with troilite (white) and graphite (black); rectangle shows an area enlarged to "D". **D.** Magnification of image "C" showing the typical appearance within an antiperthite domain. The sodium-rich host (albite) appears dark grey and contains K-feldspar exsolution lamellae (light grey).
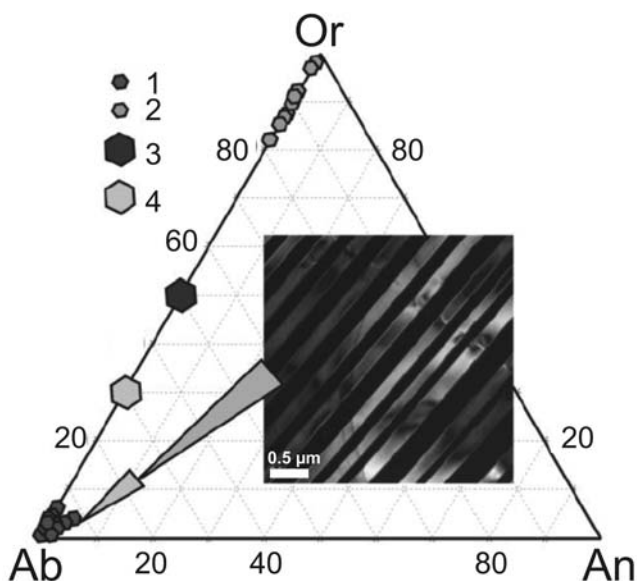
feldspar composition, the iron content is too high. Spots 6, 9, 10, and 11 have the appropriate alkali metal contents, but the silica contents are too low. Thus, all the spots are not single-phase analyses. The contaminated spots contain significant quantities of iron and some other transition metals (V, Cr, Mn, Ni, Zn, Co and Ti), chalcogens and halogens, such as S and Cl (Table 4). The less-contaminated spots show high Fe, Cr, Cl and S contents. None of these elements are compatible with a feldspar structure. The concentrations that they exhibit should not appear in feldspar. The spots (except for number 13) show noteworthy contamination due to inclusions. In turn, the lithophile elements, such as Rb,

Fig. 4. Feldspar composition (EMPA data) and microtexture. Inset image – TEM dark-field image of periodic twinning in an albite lamella in the intergrown phases (scale bar: 0.5 μm). Abbreviations: 1 – K-rich lamella in the intergrown phases, 2 – Na-rich lamella in the intergrown phases, 3 and 4 – feldspar compositions prior to coarsening (see text for explanations). The composition marked as "3" seems the most likely.
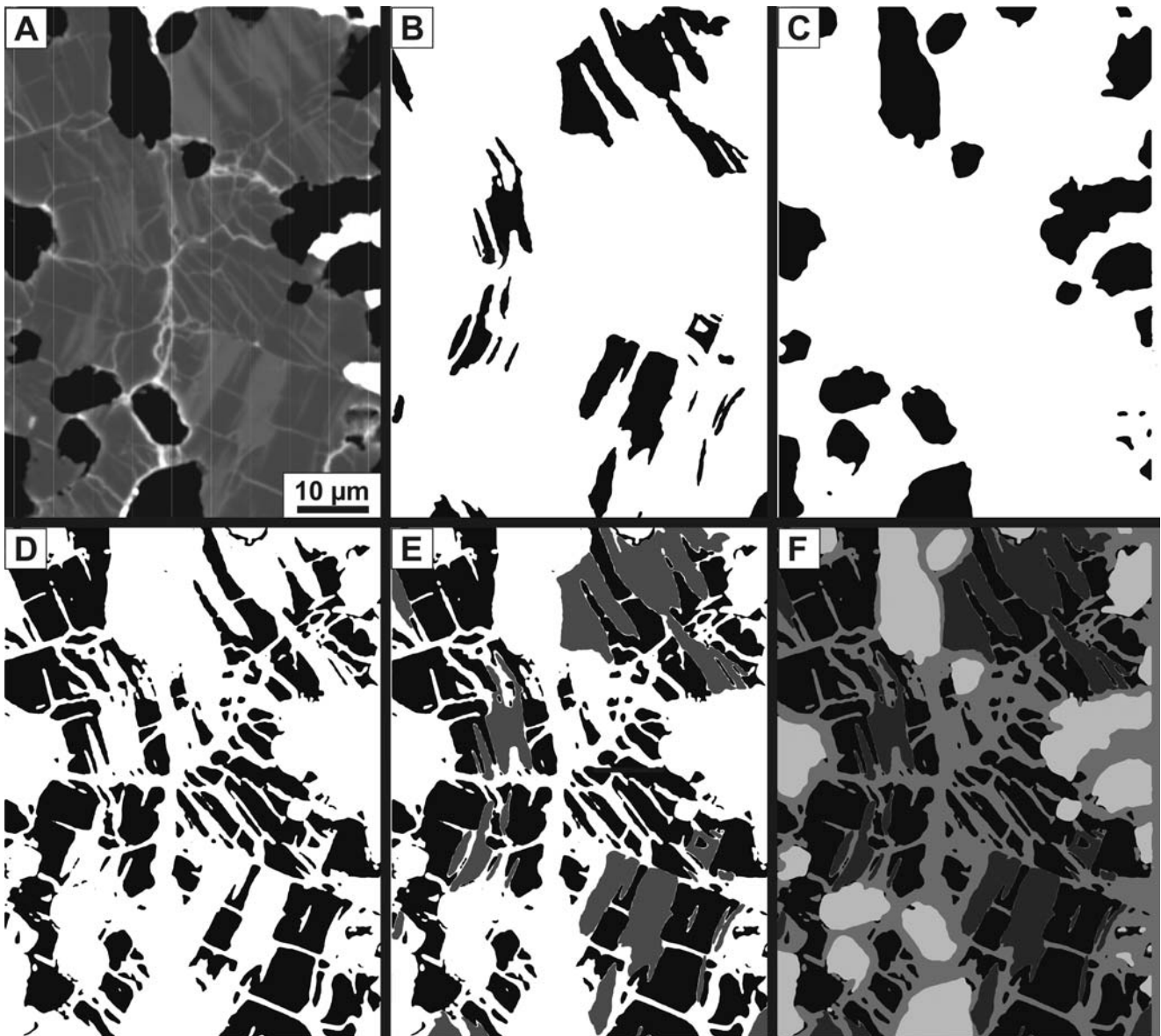
Fig. 5. Perthite/antiperthite intergrowths – image segmentation. **A.** BSE image. **B.** Or-rich domains (black). **C.** Inclusions (black). **D.** Ab-rich domains (black). **E.** Merged Or (dark grey) and Ab (black) areas. **F.** Merged Or, Ab, cracks and small intergrowth areas (light grey). On the basis of recalculation, the last category was assigned to Or-rich areas or omitted.

Sr, Ba, LREE and Pb, that usually concentrate in feldspar occur in insignificant quantities in all the spots. Because they show a stronger affinity for alkali metals than the transition elements, chalcogens and halogens, their concentration may be relevant to feldspar composition. Additionally, the LA-ICP-MS analyses performed on pyroxenes did not reveal clear enrichment in the above-mentioned elements with the exception of Cr (Table 5). LA-ICP-MS analyses of kamacite and taenite, Fe-Ni-rich minerals, were performed on unaltered areas. The analyzed taenite shows distinct enrichment in transition elements, Ga, Ge and in chlorine; kamacite is enriched in Cr (Table 6).

Raman spectra

Raman spectra from feldspar and the accompanying crystals were collected to examine their structure (Figs 6–9). The Raman spectroscopy revealed that no feldspar areas were free of inclusions. Feldspar can be identified on the basis of characteristic Raman bands at approximately 514 cm^{-1} and 480 cm^{-1} (the symmetric T-O stretch and O-T-O deformation modes in TO_4 groups), approximately 290 cm^{-1} (the O-T-O deformation and T-O-T lattice modes), and below 290 cm^{-1} (T-O-T and M-O modes) (Von Stengel, 1977). The strongest Raman bands in the 450–520 cm^{-1} spectral region belong to the ring-breathing modes of the four-membered rings of the tetrahedra. The Raman features below 400 cm^{-1} correspond to rotation-translation modes of the four-membered rings and cage-shear modes. The motion of the oxygen atoms in the breathing mode of the four-membered ring is perpendicular to the T–T line, making variations in the T–O–T bond angles a factor in determining the position of the Raman bands in the 450–520 cm^{-1} spectral region (Freeman *et al.*, 2008). Figure 6 shows a comparison of selected feldspar-rich spectra collected from within a nodule.

Table 2

Results of the electron microprobe analyses of alkali feldspars (b.d.l. – below detection limit; c.p.f.u. – cations per formula unit calculated on the basis of 8 oxygen atoms; * analyses performed within one grain)

Sample	03-3	06-2*	06-2*	06-2*	03-4	03-4	BskK	3M5	3M5	4M7	4M7	M2*	M2*	M2*
Spot	1	2a	2b	2c	4	5	6	7	8	10	11	12a	12b	12c
wt.%														
SiO_2	69.96	68.32	64.72	63.65	65.31	66.01	65.79	65.08	65.59	65.50	65.79	65.63	64.41	65.87
Al_2O_3	18.29	19.40	18.10	18.19	17.04	18.35	17.74	18.51	18.58	18.55	17.90	18.54	18.33	18.78
CaO	0.03	b.d.l.	b.d.l.	b.d.l.	b.d.l.	b.d.l.	b.d.l.	0.02	0.08	0.04	b.d.l.	b.d.l.	b.d.l.	0.02
Fe_2O_3	0.92	0.43	0.53	0.59	1.30	1.05	0.47	1.16	0.50	0.50	0.75	0.99	2.36	0.95
Na_2O	11.36	11.08	1.47	1.08	2.10	1.59	2.10	1.04	0.35	0.27	1.55	1.61	1.38	1.52
K_2O	0.29	1.10	14.55	15.14	13.61	14.80	13.85	15.07	16.29	16.36	14.03	14.77	14.39	14.33
Total	100.88	100.33	99.35	98.58	99.25	101.69	99.96	100.79	101.34	101.23	99.99	101.45	100.63	101.37
c.p.f.u.														
Si^{4+}	3.03	2.99	3.00	2.98	3.02	2.99	3.02	2.98	2.99	2.99	3.02	2.98	2.95	2.98
Al^{3+}	0.93	1.00	0.99	1.00	0.93	0.98	0.96	1.00	1.00	1.00	0.97	0.99	0.99	1.00
Ca^{2+}	0.00	0.00	0.00	0.00	0.00	0.00	0.00	0.00	0.00	0.00	0.00	0.00	0.00	0.00
Fe^{3+}	0.03	0.01	0.02	0.02	0.05	0.04	0.02	0.04	0.02	0.02	0.03	0.03	0.08	0.03
Na^+	0.95	0.94	0.13	0.10	0.19	0.14	0.19	0.09	0.03	0.02	0.14	0.14	0.12	0.13
K^+	0.02	0.06	0.86	0.90	0.80	0.86	0.81	0.88	0.95	0.95	0.82	0.86	0.84	0.83
Total	4.97	5.00	5.00	5.01	4.99	5.00	4.99	4.99	4.99	4.99	4.97	5.00	4.99	4.98
Or	1.63	6.15	86.69	90.24	81.02	85.94	81.27	90.44	96.47	97.39	85.64	85.77	87.27	86.06
Ab	98.21	93.85	13.31	9.76	18.98	14.06	18.73	9.47	3.14	2.43	14.36	14.23	12.73	13.83
An	0.16	0.00	0.00	0.00	0.00	0.00	0.00	0.09	0.39	0.18	0.00	0.00	0.00	0.11

Sample	Mor2/1*	Mor2/1*	Mor2/1*	Morbalb*	Morbalb*	Morbalb*	4M7	Mor3bis	Mor3bis	24-11	M-2	M2/2	M2/3	Mor2a
Spot	15	16	17	18	19	20	21	22	23	24	25	26	27	28
wt.%														
SiO_2	64.53	64.96	64.83	65.02	68.68	69.50	68.43	67.37	66.87	67.37	69.39	69.51	70.26	67.23
Al_2O_3	18.55	18.38	18.42	18.40	19.21	19.47	18.49	19.18	19.34	19.38	19.84	20.03	20.05	19.95
CaO	0.02	b.d.l.	b.d.l.	b.d.l.	0.01	b.d.l.	b.d.l.	b.d.l.	0.40	b.d.l.	b.d.l.	b.d.l.	b.d.l.	0.55
Fe_2O_3	0.83	1.32	0.81	1.03	0.59	0.29	2.39	0.85	0.75	0.85	0.67	0.95	0.76	0.43
Na_2O	1.25	0.91	1.19	1.14	11.30	11.25	11.22	10.89	11.14	10.89	11.62	11.79	12.24	11.17
K_2O	14.98	15.32	14.92	14.74	0.75	0.67	0.18	0.74	0.57	0.75	0.70	0.83	0.54	0.48
Total	100.06	100.82	100.12	100.23	100.48	101.15	100.47	98.95	98.98	99.15	102.19	103.04	103.80	99.77
c.p.f.u.														
Si^{4+}	2.97	2.98	2.98	2.99	3.00	3.00	2.99	2.98	2.97	2.98	2.98	2.97	2.97	2.96
Al^{3+}	1.01	0.99	1.00	1.00	0.99	0.99	0.95	1.00	1.01	1.01	1.00	1.01	1.00	1.03
Ca^{2+}	0.00	0.00	0.00	0.00	0.00	0.00	0.00	0.00	0.02	0.00	0.00	0.00	0.00	0.03
Fe^{3+}	0.03	0.05	0.03	0.04	0.02	0.01	0.08	0.03	0.02	0.03	0.02	0.03	0.02	0.01
Na^+	0.11	0.08	0.11	0.10	0.96	0.94	0.95	0.94	0.96	0.93	0.97	0.98	1.00	0.95
K^+	0.88	0.90	0.88	0.86	0.04	0.04	0.01	0.04	0.03	0.04	0.04	0.05	0.03	0.03
Total	5.00	4.99	4.99	4.98	5.00	4.98	4.98	4.99	5.01	4.99	5.01	5.03	5.03	5.01
Or	88.69	91.72	89.16	89.51	4.17	3.75	1.03	4.29	3.18	4.31	3.82	4.42	2.83	2.67
Ab	11.21	8.28	10.84	10.49	95.78	96.25	98.96	95.71	94.94	95.69	96.16	95.58	97.17	94.74
An	0.09	0.00	0.00	0.00	0.05	0.00	0.02	0.00	1.88	0.00	0.02	0.00	0.00	2.59

Results of the electron microprobe EDS analyses of Fe-Ni oxide-hydroxide veins (b.d.l. – below detection limit)

Spot	1	2	3	4	5	9	10	
	wt.%							wt.% err
SiO_2	0.18	0.74	1.10	0.13	0.13	0.15	0.05	0.01
TiO_2	b.d.l.	b.d.l.	0.03	b.d.l.	b.d.l.	b.d.l.	b.d.l.	b.d.l.
Al_2O_3	b.d.l.	0.13	0.10	b.d.l.	b.d.l.	b.d.l.	b.d.l.	b.d.l.
Cr_2O_3	0.24	12.15	14.75	0.29	0.28	0.04	0.59	0.30
FeO	92.00	77.78	73.79	92.55	93.17	95.78	67.27	0.23
MnO	b.d.l.	b.d.l.	0.07	b.d.l.	b.d.l.	b.d.l.	b.d.l.	b.d.l.
MgO	b.d.l.	b.d.l.	b.d.l.	b.d.l.	b.d.l.	b.d.l.	b.d.l.	b.d.l.
CaO	0.02	0.18	1.99	b.d.l.	0.04	0.01	b.d.l.	0.02
NiO	1.44	0.92	0.36	1.17	0.44	1.25	12.79	0.18
ZnO	0.06	0.10	0.08	b.d.l.	0.20	b.d.l.	0.14	0.14
V_2O_3	0.04	0.04	b.d.l.	0.05	0.07	b.d.l.	0.05	0.03
S	0.49	0.77	1.08	0.37	0.23	0.18	19.10	0.03
Cl	5.53	7.21	6.66	5.44	5.45	2.58	b.d.l.	0.05
Total	100.00	100.00	100.00	100.00	100.00	100.00	100.00	

The positions of the two most intense feldspar Raman bands are in the 480–482 and 511–513 cm^{-1} spectral ranges, which are similar in all the investigated images. The measured band positions and the relative intensities of the Morasko feldspar are consistent with the structure of disordered alkali feldspars. The analysis of the bands below 300 cm^{-1} indicates a degree of order. Increasing disorder results in higher intensity in the bands at 290 and 160 cm^{-1}. Assuming that the markers of disordered structure are the profiles and intensities of the 290 and 160 cm^{-1} bands, the first six spectra presented in Figure 6 represent more disordered alkali feldspar, whereas the next five spectra represent the more ordered structure of intergrown phases.

In Figure 7, the Raman spectrum shows feldspar (blue class; characteristic Raman bands at 482, 518 cm^{-1}), which co-exists with the graphite (navy-blue class) or graphite and troilite phase (violet class) (Fig. 7A–B). More detailed KMC analysis allows clear feldspar areas with variable degrees of structural order (Fig. 7C) to be found. Another compound that contaminates the feldspar-rich areas is pyroxene. The spectra in Figure 7 indicate the presence of feldspar that is mixed with graphite and pyroxene phases. The Raman spectra of feldspar presented in this work suggest the growth of feldspar crystals in the presence of graphite and pyroxene, which resulted in complex Raman features. Pyroxenes were identified on the basis of the Raman features at 339, 394, 663, 683, and 1013 cm^{-1} (Fig. 7). The most prominent Raman pyroxene band at approximately 1010 cm^{-1} is produced by the symmetric stretching vibration of Si-O_{nb} (O_{nb} represents non-bridging oxygen) within SiO_4 tetrahedra. The features in the 600–700 cm^{-1} spectral range are related to the symmetric vibrations of T-O_b-T (where T is an SiO_4 tetrahedron). A single Raman spectrum of pyroxenes is similar to that of kosmochlor-augite solid solution found in the Morasko meteorite, as presented by Karwowski et al. (2013), which is based on the detailed

analysis of the 200–1200 cm^{-1} spectral range. Small differences in the Raman band positions were observed (Wang et al., 1990; Ghose et al., 1994).

The Raman spectrum in the 1200–1800 cm^{-1} spectral range is characteristic of graphite and indicates that the graphite is disordered (Fig. 7; Ferrari and Robertson, 2001). An atypical graphite spectrum is more prominent in the detailed cluster analysis, focused on the feldspar and pyroxene phases. The results of the detailed KMC analysis with 6 clusters are presented in Figure 7D. The appearance of feldspar seems to increase the disorder in graphite symmetry (increasing the intensity of the D-band). Broad D- and G-bands, such as the ones obtained here, are characteristic of highly disordered carbonaceous materials (Tuinstra and Koenig, 1970; Wang et al., 1990; Cuesta et al., 1994; Matthews et al., 1999; Ferrari and Robertson, 2000, 2001; Escribano et al., 2001; Sato et al., 2006). Deconvolution of the D- and G-bands into Lorentzian bands D4 and D3 reveals additional bands at approximately 1240 and 1456 cm^{-1}, which can result from the presence of troilite (Fig. 7D; Table 7). Additional bands may indicate the presence of amorphous carbon in a disturbed graphitic lattice. These subtle Raman features are attributed to the presence of FeS. Figure 7D shows that the classes with graphite phases are not free of troilite. The band at 1456 cm^{-1} increases the graphite disorder and decreases the 2D-band intensity. The violet and grey clusters with the prominent troilite band intensities result in high I_D/I_G ratios, 0.552 and 0.545, respectively.

DISCUSSION

Many ideas concerning IAB formation point to a partial melting process and separation of metal from melted chondritic material (e.g., Choi et al., 1995; Mittlefehldt et al., 1998). The melting process of chondritic material generates

Table 4

Results of the LA-ICP-MS analyses performed within feldspar area (b.d.l. – below detection limit)

Spot	1	4	5	6	7	8	9	10	11	13	14	15	16
wt.%													
SiO_2	47.10	47.70	44.71	43.60	42.88	35.36	55.95	61.76	59.50	66.00	34.00	61.38	29.50
2σ	2.40	2.20	0.95	1.00	0.93	0.64	0.77	0.76	1.90	0.75	1.30	0.62	1.40
TiO_2	0.03	0.24	0.16	0.07	b.d.l.	b.d.l.	b.d.l.	b.d.l.	b.d.l.	b.d.l.	b.d.l.	b.d.l.	b.d.l.
2σ	0.01	0.03	0.03	0.01	1.00	1.00	1.00	1.00	1.00	1.00	1.00	1.00	1.00
Al_2O_3	13.54	11.51	12.46	14.55	14.78	9.51	12.81	14.64	16.68	20.45	6.60	16.79	8.14
2σ	0.94	0.53	0.60	0.42	0.38	0.21	0.33	0.29	0.57	0.45	0.37	0.29	0.37
Fe_2O_3	11.30	8.45	9.18	9.55	18.60	26.07	10.88	6.62	6.70	0.57	27.43	4.52	28.57
2σ	2.00	0.62	0.42	0.51	0.71	0.36	0.48	0.38	1.30	0.16	0.88	0.38	0.91
FeO	10.20	7.60	8.26	8.60	16.74	23.46	9.79	5.95	6.00	0.51	24.68	4.07	25.71
2σ	1.80	0.56	0.38	0.46	0.64	0.33	0.43	0.34	1.10	0.15	0.80	0.35	0.81
MnO	0.05	0.10	0.08	0.03	b.d.l.	b.d.l.	b.d.l.	b.d.l.	b.d.l.	0.01	b.d.l.	0.01	0.02
2σ	0.01	0.01	0.01	0.00	0.00	0.00	0.00	0.00	0.00	0.00	0.00	0.00	0.00
MgO	4.11	9.39	8.32	2.26	b.d.l.	b.d.l.	b.d.l.	b.d.l.	b.d.l.	b.d.l.	b.d.l.	b.d.l.	b.d.l.
2σ	0.75	0.67	0.72	0.18	1.00	1.00	1.00	1.00	1.00	1.00	1.00	1.00	1.00
CaO	b.d.l.	0.71	0.41	0.27	0.26	0.10	0.16	0.09	b.d.l.	0.11	0.07	0.05	0.05
2σ	0.00	0.31	0.17	0.16	0.05	0.06	0.04	0.03	0.03	0.09	0.05	0.02	0.05
Na_2O	5.62	5.38	5.14	5.86	5.43	4.44	8.98	9.79	9.10	9.89	5.92	11.03	4.50
2σ	0.41	0.31	0.25	0.17	0.14	0.13	0.39	0.30	0.59	0.39	0.27	0.25	0.34
K_2O	0.44	0.29	0.32	0.44	0.16	0.13	0.44	0.53	0.60	0.74	0.39	0.78	0.35
2σ	0.04	0.02	0.01	0.03	0.01	0.00	0.02	0.01	0.04	0.04	0.02	0.02	0.02
P_2O_5	0.04	0.10	0.07	0.04	0.33	0.47	0.11	0.06	0.06	0.02	0.05	0.05	0.12
2σ	0.02	0.03	0.02	0.02	0.01	0.02	0.01	0.01	0.01	0.01	0.01	0.01	0.01
SO_3	6.71	7.80	10.84	14.51	0.51	0.34	0.29	0.26	0.40	1.05	0.71	0.87	1.87
2σ	0.59	1.80	0.73	0.94	0.01	0.02	0.01	0.01	0.02	0.05	0.03	0.04	0.15
Sum	100.00	100.00	100.00	100.00	100.00	100.00	100.00	100.00	100.00	100.00	100.00	100.00	100.00
ppm													
^{35}Cl	1360	1330	740	2200	113	76	66	59	96	280	194	321	773
2σ	670	710	480	860	2	3	2	2	6	14	8	16	65
^{45}Sc	b.d.l.	0.42	2.6	1.8	b.d.l.	b.d.l.	b.d.l.	b.d.l.	b.d.l.	b.d.l.	b.d.l.	b.d.l.	b.d.l.
2σ	1	0.84	1.7	1.7	1	1	1	1	1	1	1	1	1
^{51}V	13	91	45	36	b.d.l.	b.d.l.	b.d.l.	b.d.l.	b.d.l.	b.d.l.	b.d.l.	b.d.l.	b.d.l.
2σ	4	14	8	7	1	1	1	1	1	1	1	1	1
^{53}Cr	1210	5210	3390	1780	203	136	118	105	171	494	341	544	1290
2σ	210	630	380	220	4	6	4	4	10	24	15	28	110
^{59}Co	32	54	55	39	b.d.l.	b.d.l.	b.d.l.	b.d.l.	b.d.l.	b.d.l.	b.d.l.	b.d.l.	b.d.l.
2σ	7	12	9	8	1	1	1	1	1	1	1	1	1
^{60}Ni	122	237	202	145	b.d.l.	b.d.l.	b.d.l.	b.d.l.	b.d.l.	b.d.l.	b.d.l.	b.d.l.	b.d.l.
2σ	37	80	31	36	1	1	1	1	1	1	1	1	1
^{63}Cu	101	31	63	61	b.d.l.	b.d.l.	b.d.l.	b.d.l.	b.d.l.	b.d.l.	b.d.l.	b.d.l.	b.d.l.
2σ	19	11	14	14	1	1	1	1	1	1	1	1	1
^{66}Zn	222	172	100	67	b.d.l.	b.d.l.	b.d.l.	b.d.l.	b.d.l.	b.d.l.	b.d.l.	b.d.l.	b.d.l.
2σ	86	34	23	19	1	1	1	1	1	1	1	1	1
^{71}Ga	90	74	72	106	11	12	33	60	110	141	95	146	93
2σ	11	10	8	10	1	1	2	4	6	8	6	7	6
^{73}Ge	b.d.l.	b.d.l.	b.d.l.	b.d.l.	b.d.l.	b.d.l.	b.d.l.	b.d.l.	b.d.l.	b.d.l.	1	1	2
2σ	0	0	0	0	0	1	0	0	0	0	1	1	1
^{77}Se	b.d.l.	21	17	15	b.d.l.	b.d.l.	b.d.l.	b.d.l.	b.d.l.	b.d.l.	b.d.l.	b.d.l.	b.d.l.
2σ	1	15	10	12	1	1	1	1	1	1	1	1	1

Table 4 continued

Spot	1	4	5	6	7	8	9	10	11	13	14	15	16
						ppm							
^{85}Rb	11.0	5.7	5.5	9.2	1.5	1.9	10.1	11.8	10.3	12.7	6.7	15.2	8.0
2 σ	1.9	1.3	0.8	1.5	0.2	0.3	0.7	0.5	1.2	1.2	0.7	0.8	0.8
^{88}Sr	b.d.l.	b.d.l.	b.d.l.	b.d.l.	6.2	3.9	4.6	2.8	0.3	b.d.l.	b.d.l.	0.1	b.d.l.
2 σ	0	0	0	0	0.4	0.4	0.4	0.3	0.1	0	0	0	0.1
^{98}Mo	b.d.l.	b.d.l.	b.d.l.	b.d.l.	b.d.l.	b.d.l.	b.d.l.	b.d.l.	b.d.l.	b.d.l.	b.d.l.	b.d.l.	b.d.l.
2 σ	1	1	1	1	1	1	1	1	1	1	1	1	1
^{133}Cs	b.d.l.	b.d.l.	b.d.l.	b.d.l.	0.01	0.02	0.01	0.03	0.01	0.02	0.01	0.01	b.d.l.
2 σ	0	0	0	0	0	0.01	0.01	0.01	0.01	0.02	0.01	0.01	0.01
^{137}Ba	0.2	0.0	0.5	7.2	80.0	50.1	75.5	50.9	7.7	2.0	0.4	1.5	0.4
2 σ	0.3	1.0	0.4	1.5	4.0	2.7	3.6	4.5	1.8	0.4	0.2	0.3	0.2
^{139}La	b.d.l.	b.d.l.	b.d.l.	b.d.l.	b.d.l.	b.d.l.	b.d.l.	b.d.l.	b.d.l.	b.d.l.	b.d.l.	b.d.l.	b.d.l.
2 σ	1.0	1.0	1.0	1.0	0	0	0	0	1.0	1.0	1.0	1.0	1.0
^{140}Ce	b.d.l.	b.d.l.	b.d.l.	b.d.l.	b.d.l.	b.d.l.	b.d.l.	b.d.l.	b.d.l.	b.d.l.	b.d.l.	b.d.l.	b.d.l.
2 σ	1.0	1.0	1.0	1.0	0.0	0.0	0.0	0.0	1.0	1.0	1.0	0.0	1.0
^{208}Pb	9.9	44.5	17.6	61.0	23.4	83.0	22.0	15.0	7.8	2.7	11.9	8.8	7.4
2 σ	1.2	8.1	1.4	12.0	2.8	7.5	5.1	1.7	1.0	0.5	1.0	1.4	0.6

a mafic melt and leaves an ultramafic residue (Benedix *et al.*, 2000; Takeda *et al.*, 2000; Wasson and Kallemeyn, 2002). Crystallization of the mafic melt results in plagioclase and pyroxene generation. Indeed, crystals of a plagioclase solid solution have been found by Takeda *et al.* (2000) as a product of a mafic melt segregated from an ultramafic residue. A plagioclase associated with alkali feldspar was studied by Bunch and Olsen (1968) and Wassenburg *et al.* (1968) in the Kodaikanal and Colomera iron meteorites. Plagioclase is absent from the Morasko iron meteorite. The only feldspar found is an alkali feldspar (Or-Ab solid solution).

In turn, a mixture of plagioclase of primary and secondary origin with the composition An$_{85}$-An$_5$ has been found in chondrites (Kovach and Jones, 2010; Gallegos and Jones, 2011; Jones and Brearley, 2011; Lewis and Jones, 2015; Lewis *et al.*, 2016). The wide range of composition is related to fluid-mineral interaction that caused anorthite to be replaced by albite. Potassium in the metasomatic fluid strengthens K-feldspar exsolution (Lewis and Jones, 2015; Lewis *et al.*, 2016). A similar origin for the Morasko alkali feldspar cannot be excluded definitively. However, some facts do not favour such an interpretation. In Morasko, no relic of plagioclase is present. During dissolution-re-precipitation, some of the relics should have been preserved, if the process was not going to completion, but complete replacement also cannot be excluded. In the nodules, pyroxene is replaced by kosmochlor, but relics of primary pyroxene remain. Feldspar appears in clusters of small crystals. They do not form veins, which one would expect, if the feldspar crystallized from a solution. The phase composition of Morasko points to late fluid-rock interaction, which seems to postdate alkali feldspar formation. For this reason, the present authors do not exclude metasomatism as a possible mechanism for feldspar formation. Because the origin of IAB meteorites is related to multi-stage impact-induced par-

tial melting, this discussion focuses on feldspar crystallization from mixed melts. The presence of metasomatic agents may be less likely than that of melt pockets. Wasson *et al.* (1980) and Choi *et al.* (1995) suggested that variations in the degree of impact melting alone could lead to the main observed compositional differences in IAB objects. The origin of the supposed mixed melts might have been related to interaction between the IAB projectile and the silica-rich target material. The presence of fluids may have enhanced the process.

Feldspar origin: intergrowth morphology and composition

The feldspar crystals studied form clusters, the irregular morphology of which indicates growth from small melt pockets that fill empty spaces in the nodules. They show an irregular exsolution pattern. Information that feldspar related to nodules in IAB meteorites are not homogeneous appeared in the 1960s (Bunch and Olsen, 1968). Perthite/ antiperthite intergrowths were reported by Bunch and Olsen (1968), but a photo of the intergrowths was not provided. They called the intergrowth pattern "flamboyant" and described it as "X-ray antiperthite". In the 1960s, the term "X-ray perthite" meant "perthite on a fine scale only detectable using XRD" (Parsons, personal communication).

The calculated composition of the feldspar studied is indicative of anorthoclase (according to the designation of anorthoclase composition of Smith and Brown, 1988). Crystals of such composition are homogeneous above approximately 700°C (Parsons *et al.*, 2015). Below this temperature, they immediately cross the equilibrium order solvus, resulting in exsolutions/intergrowths. During the formation of crypto-antiperthites, after volume interdiffusion of Na and K (within the Si-O-Al tetrahedral framework), a slow,

Table 5

Results of the LA-ICP-MS analyses of pyroxene
(b.d.l. – below detection limit)

Spot	1	2	3	4	5	6	7
wt.%							
SiO_2	57.27	59.42	58.84	60.01	56.76	59.26	60.33
$\pm \sigma$	1.55	1.45	1.33	1.76	3.73	1.96	1.46
TiO_2	0.11	0.15	0.09	0.07	0.32	0.15	0.21
$\pm \sigma$	0.09	0.09	0.08	0.06	0.24	0.12	0.15
Al_2O_3	0.05	0.16	2.60	0.04	0.07	0.21	0.31
$\pm \sigma$	0.00	0.01	0.05	0.00	0.01	0.01	0.03
FeO	10.69	9.34	11.85	8.14	11.61	9.28	9.19
$\pm \sigma$	0.57	0.27	0.39	0.32	0.55	0.22	0.41
MgO	31.10	30.13	24.35	30.99	29.15	30.21	28.49
$\pm \sigma$	0.48	0.53	0.34	0.67	1.21	0.46	0.65
CaO	0.63	0.50	0.39	0.61	1.21	0.55	0.75
$\pm \sigma$	0.09	0.06	0.07	0.13	0.23	0.08	0.19
Na_2O	0.14	0.27	1.77	0.14	0.85	0.29	0.57
$\pm \sigma$	0.00	0.01	0.04	0.01	0.08	0.01	0.05
K_2O	b.d.l.	0.01	0.09	b.d.l.	0.01	0.04	0.14
$\pm \sigma$	0.00	0.00	0.00	0.00	0.00	0.00	0.02
P_2O_5	0.01	b.d.l.	0.01	0.01	0.01	0.01	0.01
$\pm \sigma$	0.00	0.00	0.00	0.00	0.00	0.00	0.00
SUM	100	100	100	100	100	100	100
Norm	100	100	100	100	100	100	100
ppm							
^{23}Na	1031	2014	13167	1036	6302	2133	4259
$\pm \sigma$	35	83	303	52	624	104	360
^{27}Al	256	858	13772	229	391	1109	1622
$\pm \sigma$	19	54	254	20	37	62	169
^{31}P	60	15	30	39	52	34	65
$\pm \sigma$	15	5	8	13	15	8	13
^{34}S	2717	1764	9626	1136	16119	1821	769
$\pm \sigma$	321	257	963	302	1857	201	212
^{35}Cl	997	549	536	484	604	519	501
$\pm \sigma$	187	97	89	175	186	111	120
^{39}K	4	74	711	8	81	305	1128
$\pm \sigma$	1	7	27	3	23	21	134
^{43}Ca	4484	3590	2798	4348	8623	3934	5358
$\pm \sigma$	656	444	502	912	1658	554	1340
^{45}Sc	13	13	9	14	11	14	10
$\pm \sigma$	1	1	1	2	3	1	2
^{47}Ti	650	919	569	410	1937	893	1234
$\pm \sigma$	39	42	24	35	259	38	106
^{51}V	38	52	45	39	207	62	101
$\pm \sigma$	2	2	2	2	28	2	11
^{53}Cr	2356	3118	2503	2349	9287	3414	6571
$\pm \sigma$	94	104	96	84	1128	139	451
^{55}Mn	2168	2353	1938	2210	2235	2282	2291
$\pm \sigma$	66	52	38	68	86	48	85
^{59}Co	24	8	32	3	74	5	7
$\pm \sigma$	5	1	5	1	9	1	1

Table 5 continued

Spot	1	2	3	4	5	6	7
ppm							
^{60}Ni	133	54	213	3	207	13	19
$\pm \sigma$	23	9	26	2	26	2	3
^{63}Cu	3	4	17	b.d.l.	42	2	b.d.l.
$\pm \sigma$	1	1	3	0	8	1	0
^{66}Zn	787	946	947	847	856	865	1022
$\pm \sigma$	32	37	28	46	80	34	56
^{71}Ga	2	6	31	1	7	4	6
$\pm \sigma$	0	1	2	0	1	1	1
^{90}Zr	1	2	1	2	1	10	21
$\pm \sigma$	0	0	0	0	0	1	3
^{209}Bi	0.12	0.05	0.20	b.d.l.	0.08	0.01	0.01
$\pm \sigma$	0.03	0.01	0.07	0.00	0.02	0.00	0.01
^{75}As	b.d.l.	b.d.l.	b.d.l.	b.d.l.	b.d.l.	b.d.l.	b.d.l.
^{121}Sb	b.d.l.	b.d.l.	b.d.l.	b.d.l.	b.d.l.	b.d.l.	b.d.l.

diffusive phase transition proceeds, involving Si-Al ordering (Smith and Brown, 1988; Part 4). Such ordering that leads to continuous change from triclinic high albite to low albite occurs while still at a high temperature, ranging from 700 to 650°C (Parsons *et al.*, 2015). Raman spectra collected on the feldspar studied indicate an ordering process and show that the process was not completed. The spectra suggest a structure, consisting of domains of disordered with domains of a partly ordered structure. Raman band positions characteristic of completely ordered sodium-rich feldspar (455 cm^{-1}) were not observed in the Morasko feldspar. Owing to the presence of other crystals and a relatively low signal-to-noise ratio, the Raman features typical for an ordered structure at approximately 760 and 815 cm^{-1} (tetrahedral deformation) also were not observed. For the spectra presented in Fig. 6, the calculated I515/I480 ratio of 2.54±0.26 indicates a more disordered structure. In addition to the triplet bands, the bands above 600 cm^{-1} denote tetrahedral framework deformation. The Raman band at 577 cm^{-1} (Fig. 8) is a result of *ac*-plane translations (Si, Al-tetrahedral deformations) and Na coordination deformation (O-Na-O bending; McKeown, 2005). Less intense Raman features observed in the 1100–1200 cm^{-1} spectral range (Fig. 8) indicate mixtures of Si-O and Al-O stretching, as well as O-Si-O and O-Al-O bending (McKeown, 2005). The average spectrum of feldspar in the measured area shown in Fig. 7 is comparable to a single previously presented spectrum of albite (Karwowski *et al.*, 2013).

The antiperthite intergrowths consist of Na-rich and K-rich feldspar with slightly varying composition. The albite-rich lamellae in the intergrown phases become more extreme (with a negligible amount of Or), whereas the orthoclase-rich lamellae in the intergrown phases exhibit larger variability (a more significant Ab content). Neither the Na-rich nor K-rich lamellae in the intergrown phases reach the pure end-member composition of Ab or Or. During exsolution, progress toward the approach of pure end-member composition by Na-rich and K-rich lamellae is corre-

Table 6

Results of the chemical analyses of kamacite and taenite (LA-ICP-MS data; all values are given in ppm; average Fe content in Morasko kamacite – 95 wt.%, taenite – 70 wt.%; b.d.l. – below detection limit)

	Kamacite	Kamacite	Kamacite	Taenite	Taenite	Taenite
^{23}Na	20	12	11	1	b.d.l.	b.d.l.
^{24}Mg	6	4	b.d.l.	b.d.l.	b.d.l.	b.d.l.
^{27}Al	3	4	b.d.l.	b.d.l.	b.d.l.	1
^{29}Si	492	380	b.d.l.	744	991	273
^{31}P	106	269	68	232	254	706
^{34}S	503	517	322	223	339	430
^{35}Cl	18888	20308	1341	1652	554	991
^{39}K	15	8	b.d.l.	10	b.d.l.	13
^{43}Ca	738	1207	22353	1281	1198	1355
^{49}Ti	3	b.d.l.	b.d.l.	b.d.l.	b.d.l.	b.d.l.
^{51}V	b.d.l.	b.d.l.	b.d.l.	1	b.d.l.	1
^{53}Cr	132	164	126	12	7	31
^{55}Mn	36	37	42	32	30	25
^{59}Co	1383	1323	1006	1914	2074	2640
^{60}Ni	16731	15379	15558	158303	175654	124511
^{63}Cu	1	2	1	599	720	427
^{66}Zn	37	11	b.d.l.	145	144	89
^{71}Ga	b.d.l.	b.d.l.	1	148	189	154
^{73}Ge	b.d.l.	b.d.l.	b.d.l.	365	469	466
^{75}As	b.d.l.	b.d.l.	b.d.l.	5	7	7
^{85}Rb	b.d.l.	b.d.l.	b.d.l.	b.d.l.	b.d.l.	b.d.l.
^{88}Sr	b.d.l.	b.d.l.	b.d.l.	b.d.l.	b.d.l.	b.d.l.
^{89}Y	b.d.l.	b.d.l.	b.d.l.	b.d.l.	b.d.l.	b.d.l.
^{90}Zr	b.d.l.	b.d.l.	b.d.l.	b.d.l.	b.d.l.	b.d.l.
^{93}Nb	b.d.l.	b.d.l.	b.d.l.	b.d.l.	b.d.l.	b.d.l.
^{98}Mo	21	31	22	27	27	21
^{111}Cd	b.d.l.	b.d.l.	b.d.l.	b.d.l.	b.d.l.	b.dle.
^{118}Sn	b.d.l.	b.d.l.	b.d.l.	6	10	7
^{121}Sb	b.d.l.	b.d.l.	b.d.l.	b.d.l.	b.d.l.	b.d.l.
^{137}Ba	b.d.l.	b.d.l.	b.d.l.	b.d.l.	b.d.l.	b.d.l.
^{195}Pt	b.d.l.	b.d.l.	b.d.l.	7	7	7
^{197}Au	b.d.l.	b.d.l.	b.d.l.	2	3	2
^{205}Tl	b.d.l.	b.d.l.	b.d.l.	b.d.l.	b.d.l.	b.d.l.
^{206}Pb	b.d.l.	13	b.d.l.	b.d.l.	b.d.l.	b.d.l.
^{209}Bi	b.d.l.	b.d.l.	b.d.l.	b.d.l.	b.d.l.	b.d.l.
^{232}Th	b.d.l.	b.d.l.	b.d.l.	b.d.l.	b.d.l.	b.d.l.
^{238}U	b.d.l.	b.d.l.	b.d.l.	b.d.l.	b.d.l.	b.d.l.

Table 7

Raman parameters of the fitted D and G bands of carbon (FWHM stands for full width at half maximum, in cm^{-1})

Raman spectrum	Raman band position [cm^{-1}]	Assignment	Raman intensity [a.u.]	FWHM	Integral
gray class	1238	D4	0.04	87.90	5.17
	1345	D1	0.12	118.84	22.58
	1457	D3	0.09	132.38	17.97
	1571	G	0.22	97.17	33.90
	2678	2D	0.02	80.54	2.13
orange class	1345	D1	0.10	87.00	13.69
	1462	D3	0.07	142.44	16.52
	1575	G	0.21	83.00	27.18
	2686	2D	0.02	105.38	3.22
red class	1265	D4	0.03	130.22	6.28
	1348	D1	0.12	71.40	12.90
	1458	D3	0.09	145.80	20.17
	1576	G	0.22	81.17	28.05
	2688	2D	0.03	113.12	4.51
violet class	1241	D4	0.03	75.96	3.70
	1344	D1	0.12	117.90	21.97
	1455	D3	0.09	137.72	19.18
	1572	G	0.21	97.52	32.90
	2674	2D	0.01	60.67	1.14

lated with an increasing order in their Si-O-Al framework (Parsons *et al.*, 2015). The Morasko alkali feldspar crystals are almost anorthite-free. In such crystals, alkali volume interdiffusion is very fast because there is no need for a coupled move with Al^{3+} in the framework (Smith and Brown, 1988; Parsons *et al.*, 2015). The volume exchange of alkali metals causes equilibration with respect to Na-K, but the crystals may not be equilibrated fully with respect to Al-Si (McDowell, 1986). Thus, the cooled crystals may preserve

their disordered structure, which is documented in the Raman spectra.

The morphology of coherent intergrowths is related to polysynthetic twinning (Willaime and Brown, 1974; Brown and Parsons, 1988). Incoherent intergrowths result from replacement reactions (Parsons and Lee, 2009; Parsons *et al.*, 2009, 2015). Foils for the TEM study could be cut only from the Na-rich lamellae in the intergrown phases. The attempt to cut a foil from a K-rich lamella in the intergrown phases failed. A TEM image of a Na-rich lamella in the intergrown phases shows a perfectly twinned crystal with regular lamellae and sharp boundaries. The lamellae do not have any dislocations. The regularity in twinning morphology indicates that there was no process of later modification, e.g., visible grain boundary interactions or replacive interactions (Parsons and Lee, 2009; Parsons *et al.*, 2015). The Raman spectra of feldspars are not sensitive to Na and K content and do not differ significantly (Freeman *et al.*, 2008). Thus Raman imaging of Na-rich and K-rich lamellae in the intergrown phases specifies only the Si-Al order or disorder of their structures. Raman spectra of all measured domains show a dominance of a disordered feldspar pattern over an ordered one. Taking into account existing knowledge of the transformation of K-rich lamellae in the intergrown phases in antiperthite, the present authors speculate that K-rich lamellae would not show an advanced stage of the development of a tweed microstructure.

The morphology of perthite/antiperthite lamellae depends on the thermal history (Smith and Brown, 1988) and
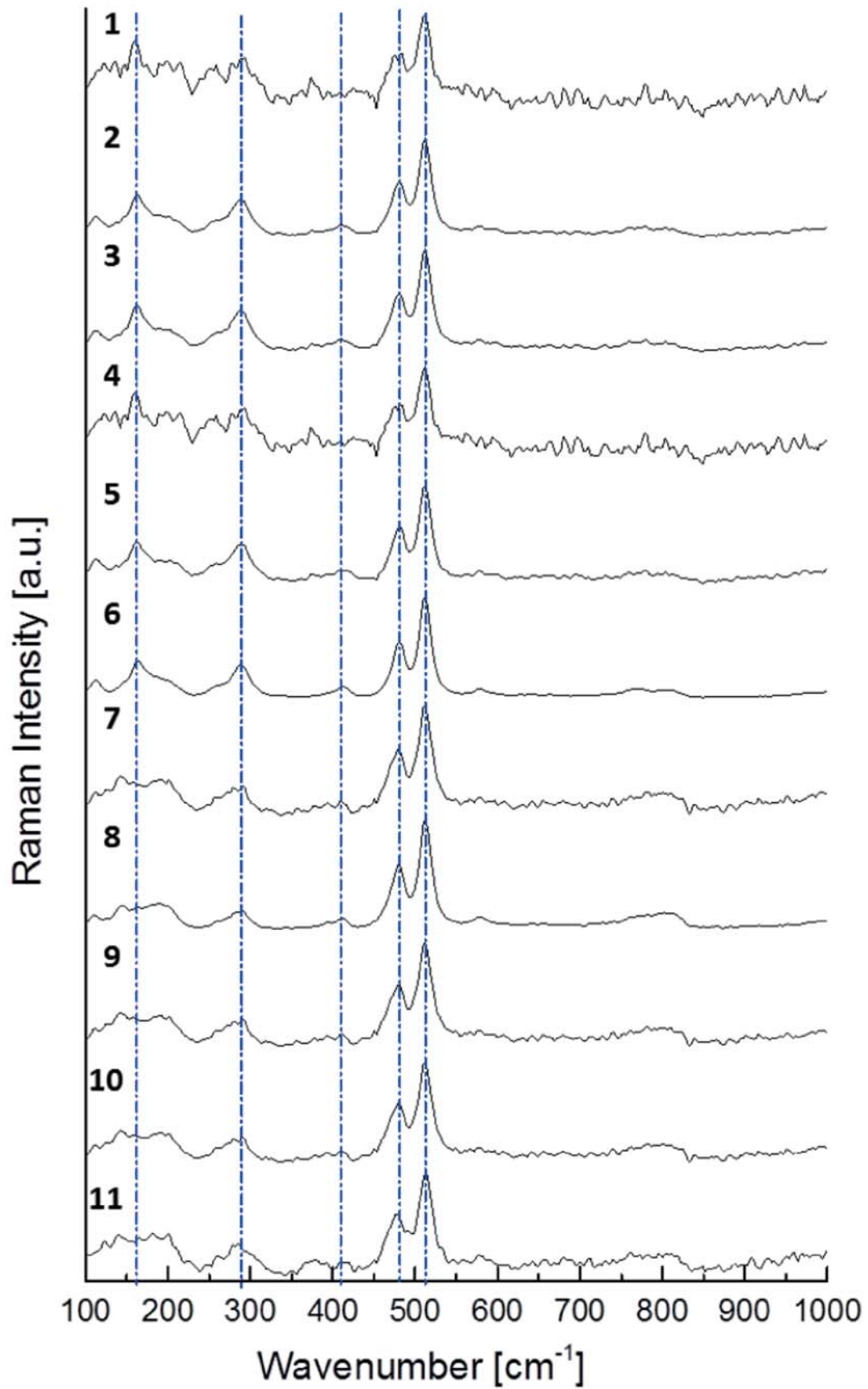
Fig. 6.   Selected Raman spectra collected from feldspar-rich areas (dash-dot lines represent the positions of Raman bands at 162, 289, 410, 480, and 512 cm^{-1}).

growth rate (Buerger, 1945; Vance, 1961; Donelly, 1967; Słaby, 1992). The Morasko Ab-rich feldspar with an anti-perthitic microstructure probably crystallized at a high temperature (far above 700°C). During cooling, it passed through a structure transition, probably occurring within the temperature range 700–650°C. However, the transformation process was incomplete. It seems that at some stage in the transformation, the increasing cooling rate inhibited further effective Si and Al diffusion in the tetrahedral framework. Also, the interdiffusion process in the crystals studied does not approach full equilibration with respect to the alkali metals. This lack of full equilibration caused variable Ab-to-Or ratios in the antiperthite lamellae after exsolution. Thus, the antiperthite composition, microtexture and structure order-disorder may be consistent with a thermal history, indicative of rapid cooling, maybe combined with degassing of the system at some stage of phase transition. Lack of volatile substances slows down the phase transition process. The disordered structure of graphite that accompanies feldspar might be explained similarly. Such a thermal history is compatible with the Wasson and Kallemeyn (2002) model that supposes crystallization under conditions of rapid heating and cooling. Another explanation of the feldspar microstructure demonstrating a more disordered structure is secondary shock-induced disordering. This hypothesis can account for a perthite/antiperthite pattern in the Morasko nodules, which is described as "flame perthite" (Pryer and Robin, 1995, 1996). "Flame perthite" is usually interpreted as being caused by exsolution during external deformation, in a field involving high differential stress. However, the different orientation of intergrown phases in neighbouring crystals argues against this origin of intergrowths. In addition, shock-induced disordering should result in a partial isotropization of feldspar structure as well as textures compatible with shock (Stöffler *et al.*, 1991). Neither a signature of isotropization of the feldspar structure in Raman spectra nor shock textures were observed.

The present paper shows for the first time an image of an antiperthite pattern in an IAB nodule. The authors present the data without advocating any specific mechanism for intergrowth formation. The present interpretation of the intergrown phases was made on the basis of data obtained for terrestrial alkali feldspar. The Morasko feldspars contrast with terrestrial feldspars. The low anorthite content of the Morasko feldspars is very unusual, although An is mainly partitioned into the Ab-rich lamellae, indicating that the distribution of An and Ab represent equilibrium (Parsons, personal communication). However, the intergrowths cannot have formed by exsolution. Rather, they may have formed by simultaneous growth at a very high P (Goldsmith and Newton, 1974; Parsons, 1978). At very high P, the feldspar solvus moves to higher temperatures, thus allowing the growth of two phases simultaneously. The fact that the alkali feldspars are disordered because of rapid cooling supports this hypothesis.

Melt composition

Assuming the feldspar is of magmatic origin, its crystallization requires a melt rich in both alkali metals and silica.
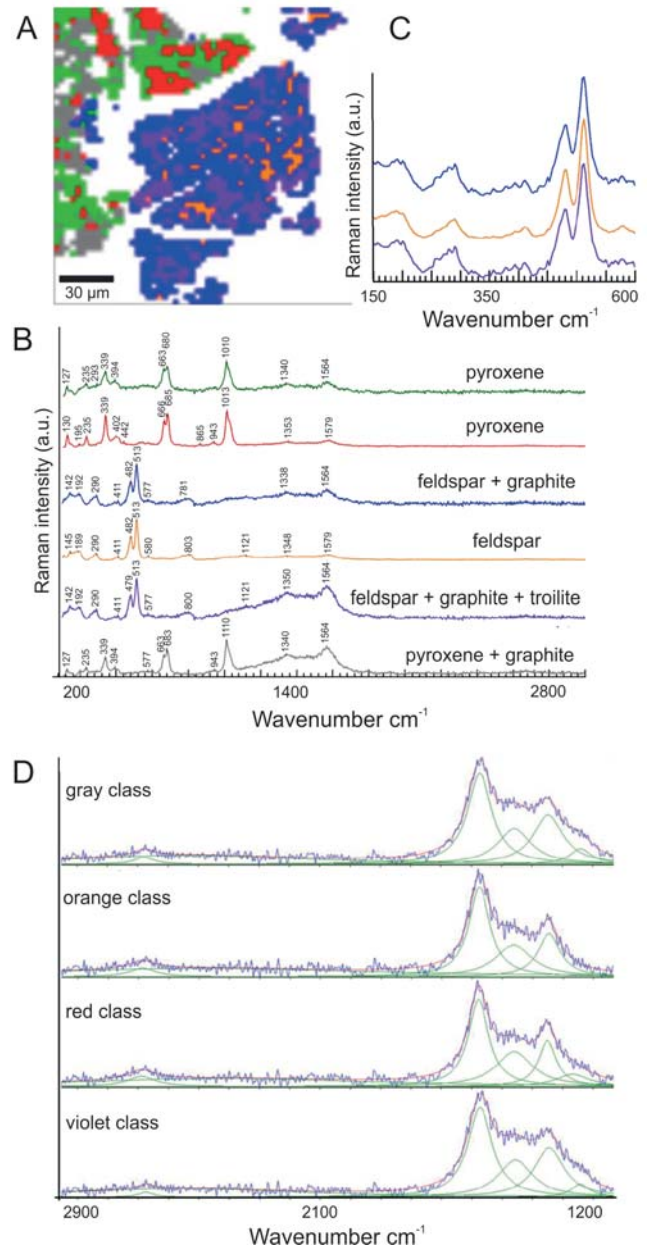
Fig. 7. Detailed KMC analysis obtained by the application of k-means cluster algorithm to areas rich in feldspar and pyroxene phases. **A.** Green and red clusters – pyroxenes, blue class – feldspar and graphite, orange class – feldspar (ordered albite), violet class – mixture of feldspar (ordered albite), and graphite, and grey class – pyroxene and graphite). **B.** The average spectra of clusters presented at the figure A. **C.** Magnification of typical feldspar bands; selected Raman spectra from B fitted following a linear baseline correction. **D.** A Lorentzian band model.

In the Morasko nodules, the alkali feldspar is accompanied by three types of pyroxene: enstatite, a kosmochlor-augite solid solution and kosmochlor itself. The Raman images collected in the present study confirm the presence of an alkali feldspar – kosmochlor-augite association. Unlike the composition of enstatite, which is constant, the kosmochlor-augite solid solution and kosmochlor (both rich in alkali metals) exhibit a large variation in composition (Karwowski and Muszyński, 2006). In addition, different pro-

portions of the same phase are observed in different nodules. In certain nodules, feldspar occurs with enstatite. Nodules with kosmochlor and feldspar do not contain any enstatite. The kosmochlor-augite solid solution occurs with enstatite and exhibits textures compatible with replacement. Enstatite appears to have been replaced by the kosmochlor-augite solid solution and then finally by kosmochlor (Karwowski *et al.*, 2015). The studied clusters of feldspar classified as anorthoclase contain very low concentrations of all LIL (Ba, Rb, Sr, Pb, and LREE) elements that show a strong affinity for silicates. The feldspar composition, the mineral association, in which it occurs, and the proportions of individual phases in the association are sources of important information about the melt origin and its evolution.

Many authors relate the silicate presence in IAB meteorites to a partial melting process of chondritic material (Choi *et al.*, 1995; Mittlefehldt *et al.*, 1998; Benedix *et al.*, 2000; Takeda *et al.*, 2000; Wasson and Kallemeyn, 2002). Assuming that partial melting leaves an ultramafic residue (olivine and orthopyroxene) and generates a mafic melt, this melt should have led to the appearance of Ca-pyroxene (diopside) and plagioclase (Takeda *et al.*, 2000). The present authors have not observed any plagioclase or pyroxene with any appropriately calcium-rich compositions in the Morasko meteorite. The mafic component is missing. Experiments with shock-melting of chondritic material (as a target) with alkali metal concentrations below 2 wt.% result in melt depletion in alkali metals (below 1 wt.%; Hörz *et al.*, 2005). Thus, only a residual highly fractionated melt derived from such parental melt should have led to alkali feldspar crystallization. However, Wasson and Kallemeyn (2002) excluded fractional crystallization as a mechanism, causing silicate-melt evolution in IAB meteorites. In addition, trace element concentrations in the alkali feldspar do not confirm such a process. The low degree of melting of ultramafic material results in melt enrichment in incompatible elements (e.g., McKenzie and O'Nions, 1991; Peccerillo *et al.*, 2003, 2013; Upton *et al.*, 2013). The concentrations of LIL elements, which are concentrated preferentially in alkali feldspar (spot 13), are low. Only Ga shows an unexpectedly high concentration. An average Ga concentration in feldspar is in the range of 18–29 ppm (Deer *et al.*, 2001). In the Morasko feldspar, the estimated concentration is almost five times larger and probably resulted from inclusions (taenite) present within the spot analyzed. Assuming that alkali feldspar is a product of crystallization of a highly evolved fractionated melt, the progressive evolution of parental melt (already enriched in incompatible elements) should make it even richer in these elements and remove from it compatible elements (Peccerillo *et al.*, 2003, 2013; White *et al.*, 2009; Upton *et al.*, 2013). However, partition coefficients that describe trace element partitioning in terrestrial and meteorite melt-generating settings may not be equivalent. Good indicators of mafic melt evolution are Rb and LREE, incompatible during FC and incompatible, except for Eu, for alkali feldspar. The rubidium concentration is low and the LREE concentrations are below the detection limit in the Morasko feldspar. In turn, strontium is compatible with feldspars and behaves as a compatible element during parental melt evolution. A highly fractionated melt is

depleted in Sr. Despite this, its concentration in the Morasko feldspar is unexpectedly low. The major and trace element composition of feldspar from Morasko cannot be the product of crystallization of a parental melt, extracted from a chondritic source and evolved by fractional crystallization. Alkali feldspar is associated with Na-Cr-rich pyroxenes (Karwowski and Muszyński, 2008). Karwowski and Muszyński (2008) studied the origin of pyroxene crystals and related their appearance to two different silicate melts. According to their hypothesis, the first melt crystallized enstatite and olivine. The second melt gave rise to kosmochlor. Being rich in Ca, Na and Cr, the melt reacted with the previously formed enstatite, leading to a kosmochlor-augite solid solution. During the process of crystallization of chromite, the residual melt led to the crystallization of another kosmochlor-augite solid solution, which was richer in Na and Cr. Taking into consideration the discussion presented above, the enstatite-olivine association should likely be interpreted as an ultramafic residue after chondrite melting. The most interesting problem arising from the discussion of the appearance of pyroxene is the origin of the Na-Cr-rich melt. Multiple impact events, inducing melting/remelting, may lead to progressive partial-melt enrichment in silica and alkali metals. Wasson and Kallemeyn (2002) argued that IAB formation involves both crystal segregation, in which the solids and melts are basically in equilibrium, and multiple impact-generated melting events that create the different subgroups. These processes may control the crystallization of the above-mentioned silicate succession: kosmochlor-augite solid solution, kosmochlor and finally alkali feldspar. However, each partial-melting event of the silicate-bearing source should leave traces of an appropriate residual solid, which is not observed in the nodules investigated. Assuming that the enstatite–olivine association is the residue of a mafic melt generation, the next partial melting event removes these mafic melt crystallization products and yields an alkali- and silica-enriched melt. The partial melting of the mafic association leaves different residua depending on the temperature and pressure; however, all residua should contain Ca-Mg pyroxene (Rapp and Watson, 1995), which is not found in the nodules. Thus, even if the nodule phase composition could be explained by multi-event melting, there is no convincing evidence supporting this hypothesis. An additional melt source is needed. Such a source may be the target material interacting with the IAB projectile during impact (Ebert *et al.*, 2013, 2014; Hamann *et al.*, 2013). The experiment done by Ebert *et al.* (2013) showed that during the hypervelocity impact of a steel projectile with a silica-rich target (quartzite, sandstone), melting of both the projectile and the target material is observed. Significant mixing (chemical and mechanical) of target material with projectile accompanies the process. The trace element partitioning between the steel projectile and the contaminated target melt explains why trace element ratios in the metal projectile differ from ratios in contaminated target melts. Do the phase and chemical compositions of the Morasko nodules corroborate this hypothesis?

Many pieces of information on the nodule's late-stage crystallization involve the transition trace elements, chlorine and sulphur, found in the analyzed feldspar areas. It

seems that the spots analyzed, even if carefully located within feldspar, corresponded with inclusions and a multi-phase mixture of veins cutting across the nodules and interconnecting areas of silicates with troilite inclusions. The elements found in the spots are not compatible with the feldspar crystallization process, yet they are observed in large concentrations. However, they are typical elements in Fe-Ni oxide-hydroxide (Table 3). Two of the particularly interesting elements found in the veins are iron and chlorine. No primary minerals containing chlorine have been identified within the nodules, but outside the nodules, the chlorine-bearing mineral djerfisherite has been recognized (Karwowski and Gurdziel, 2009). An akaganeite – iron oxide-hydroxide/chloride mineral was identified as an alteration product of taenite and kamacite (Karwowski and Gurdziel, 2009). Kamacite and taenite (the exsolution products of the Fe-Ni metal phase), without any visible sign of alteration, show a distinct enrichment in the transition elements, as well as in Cl. This indicates that the late alteration process commonly occurs even in an apparently fresh metallic part of the meteorite (Table 6). Thus, the veins in the nodules seem to share similar chemical characteristics with the Fe-Ni metal host, but with a lower concentration of Ni. Nevertheless, small relics of Fe-Ni metal are preserved within mixtures of secondary minerals (Table 3). Another iron-rich phase is troilite. Troilite inclusions are easily visible in the feldspar clusters. Troilite develops intergrowths with graphite (Karwowski and Muszyński, 2008). Troilite inclusions may be related to FeS melt droplets. Thus, crystallizing silicate and sulphide were associated with a Fe- and Ni-rich melt appearing in the veins. This means that the whole association requires silicate- sulphide and metal melts. The Raman images (Figs 7–9) show an assemblage of silicate together with troilite and the metal-rich phase. Benedix *et al.* (2000) assumed that the occurrence of partial melting and metal and FeS separation in IAB meteorite followed by the development of an impact-generated silica-metal mixture. Troilite metal is more easily melted than are silicates during impact (Wasson and Kallemeyn, 2002). During impact experiments between steel projectiles and silica-rich targets, the silica-rich target melts are strongly enriched in the projectile trace elements (Ebert *et al.*, 2014). Iron is preferentially introduced into the target melt to a greater degree than Ni and Co are (White, 2013; Ebert *et al.*, 2013, 2014). Molybdenum and tungsten are sparse in the target melt (Ebert *et al.*, 2014). The silicate melt is relatively enriched in V and Cr (Ebert *et al.*, 2014). Variations of Fe, Ni, Co, V and Cr partitioning are associated with the selective behaviours of these elements (White, 2013). In the veins, the Ni concentration is lower than in the kamacite-taenite intergrowths. The spots analyzed are rich in Cr and depleted in V. Chromium as Cr-rich spinel is very likely to be associated with the Fe-Ni oxide-hydroxide veins, with the daubreelite inclusions in troilite, and with pyroxene: kosmochlor-augite and kosmochlor. Taking into consideration the composition of feldspar, including its inclusions and veins, it is very likely that the whole mineral assemblage may be achieved by crystallization of a sulphide, a metal and a variably contaminated mafic melt. The contaminant may be related to a silica-rich impact target melt. Mechanical and chemical mix-

ing of these three very different melts does not result in homogenization. Drops of metallic and sulphide melt tend to separate in a silicate melt, because they are immiscible. The emulsion of these melts either crystallizes simultaneously, or it may result in veins of Fe-Ni metal filling the cracks with some delay. In the Chelyabinsk meteorite, albite-affine crystals and irregular nests of albite-affine glass have been found in the incompletely crystallized melt, derived by the interaction with the silica-rich target (Richard Wirth unpublished data). Both domains, crystalline and amorphous, contain numerous inclusions of Cr-rich spinel, troilite, and drops of Fe-Ni melt. Impact melting and mechanical mixing of liquids is considered to have been responsible for feldspar crystallization in the Maniitsoq structure (Garde and Keulen, 2013).

An ultramafic mineral assemblage coexisting with silica-rich melt may have resulted from the interaction of an iron meteorite projectile with sand or sandstone target material during the impact event, according to Hamann *et al.* (2013). They reported a poorly polymerized, ultrabasic melt (rich in Fe^{2+}, Ca^{2+} or Mg^{2+}) dispersed in a highly polymerized high-silica melt matrix from the Wabar craters (Saudi Arabia). The first melt may lead to olivine-enstatite, the second melt to feldspar crystallization. The crystallization sequence in the Morasko nodules appears to be similar.

The origin of the sequence might be different. The ultramafic association did not crystallize simultaneously; rather, it preceded feldspar crystallization. Olivine and enstatite might be ultramafic residua after the impact-related generation of the mafic melt that is contaminated by the silica-enriched impactor material. The variability in the sodium-enriched mineral compositions might be related to variable degrees of mafic impact-melt interaction with the target material. Consequently, the assemblage studied implies the probable collision of a IAB host and a silicate impactor. This process may cause partial remelting of the Fe-Ni-metal and ultramafic/mafic-silicate host and mixing with the partial melts from the silicate impactor. The variable proportions of different phases in different nodules may be evidence for material mixing, e.g., solid with melt or melt with re-melted material, related to the asteroid disruption process (Ruzicka *et al.*, 1999; Benedix *et al*., 2000; Takeda *et al.*, 2000; Wasson and Kallemeyn, 2002; Goldstein *et al*., 2009). Mixing, owing to its chaotic nature, also induces variability in mineral compositions and abundances of individual phases (Perugini *et al*., 2006; De Campos *et al*., 2011; Perugini and Poli, 2012). This can cause variations in the kosmochlor-augite solid solution and kosmochlor compositions, as well as in the quantity of their crystals accompanying the alkali feldspar in various nodules.

CONCLUSIONS

1) Alkali feldspar crystals have been recognized in the troilite-graphite nodules of the Morasko IAB iron meteorite. The data are in support of their crystallization from melt.

2) The melt that crystallized the feldspar cannot be related to impact-induced partial melting of the chondritic material alone.

3) The emergence of an assemblage of alkali feldspar with Na-Cr-rich pyroxene, sulphide inclusions and Fe-Ni oxide-hydroxide veins in nodules might be indicative of the presence of three immiscible melts: metal, sulphide and silicate. It indicates interaction between the IAB projectile and a silica-rich target material. A parental melt derived from chondritic material and contaminated by the melt derived from the target material possibly led to feldspar crystallization. Low LIL element concentrations in the feldspar corroborate such a hypothesis.

4) The feldspar composition is similar to anorthoclase, which produced exsolution patterns during the cooling process. The disordered structure preserved may be related to the cooling history of the crystals or to secondary shock-induced disordering. Because no isotropization is observed in feldspar structures, the first hypothesis is more probable.

5) The present study reports for the first time the pattern of antiperthite intergrown with phases in an IAB meteorite. Further research, however, is needed to explain the detailed mechanism of pattern formation.

6) The varying composition and quantity of the kosmochlor-augite solid solution and kosmochlor in different nodules can also be linked to variable degrees of melt interaction/contamination.

7) The silicate melt pockets (crystallizing alkali feldspar and Na-Cr-rich pyroxene) with interconnecting metal melt veins simultaneously crystallized with droplets of sulphide melt (troilite).

8) Concentrations of transition elements (especially Fe, Ni, Cr) measured in the Fe-Ni oxide-hydroxide veins correlate with element redistribution during interactions between the metal projectile and the silica-rich target material.

REFERENCES

Benedix, G. K., Lauretta, D. S. & McCoy, T. J., 2005. Thermodynamic constrains for formation conditions of winonaites and silicate-bearing IAB irons. *Geochimica et Cosmochimica Acta*, 69: 5123–5131.

Benedix, G. K., McCoy, T. J., Keil, K. & Love, S. G., 2000. A petrologic study of the IAB iron meteorites: constraints on the formation of the IAB–Winonaite parent body. *Meteoritics & Planetary Science*, 35: 1127–1141.

Brown, W. L. & Parsons, I., 1988. Zoned ternary feldspars in the Klokken intrusion: Exsolution textures and mechanisms. *Contributions to Mineralogy and Petrology*, 98: 444–454.

Buerger, M. J. 1945. The genesis of twin crystals. *American Mineralogist*, 30: 469–482.

Bunch, T. E. & Olsen, E., 1968. Potassium Feldspar in Weekeroo Station, Kodaikanal, and Colomera Iron Meteorites. *Science*, 160: 1223–1225.

De Campos, C. P., Perugini, D., Ertel-Ingrisch, W., Dingwell, D. B. & Poli, G., 2011. Enhancement of magma mixing efficiency by chaotic dynamics: an experimental study. *Contribution to Mineralogy and Petrology*, 161: 863–881.

Choi, B.-G., Ouyang, X. & Wasson, J. T., 1995. Classification and origin of the IAB and IIICD iron meteorites. *Geochimica et Cosmochimica Acta*, 59: 593–612.

Cuesta, A., Dhamelincourt, P., Laureyns J., Martinez-Alonso, A. & Tascon, J. M. D., 1994. Raman microprobe studies on carbon materials, *Carbon*, 32:1523–1532

Deer, W. A., Howie, R. A. & Zussman, J., 2001. *Rock-forming Minerals, vol. 4A. Framework Silicates, Feldspars*. The Geological Society, London, 972 pp.

Dominik, B. 1976. Mineralogical and chemical study of coarse octahedrite Morasko. *Prace Mineralogiczne PAN*, 47: 7–53.

Donnelly, T. W., 1967. Kinetic considerations in the genesis of growth twinning. *American Mineralogist*, 52: 1–12.

Dziel, T., Gałązka-Friedman, J. & Karwowski, Ł., 2007. Mössbauer investigations on Marlow and Morasko meteorite. *IIIrd Meteorite Seminar 21–22.04.2005, Olsztyn*. Olsztyńskie Planetarium i Obserwatorium Astronomiczne, Polskie Towarzystwo Meteorytowe, pp. 17–23. [In Polish, with English abstract.]

Ebert, M., Hecht, L., Deutsch, A. & Kenkmann, T., 2013. Chemical modification of projectile residues and target material in a MEMIN cratering experiment. *Meteoritics & Planetary Science*, 48: 134–149.

Ebert, M., Hecht, L., Deutsch, A., Kenkmann, T., Wirth, R. & Berndt, J., 2014. Geochemical processes between steel projectiles and silica-rich targets in hypervelocity impact experiments. *Geochimica et Cosmochimica Acta*, 133: 257–279.

Escribano, R., Sloan, J. J., Siddique, N., Sze, N. & Dudev, T., 2001. Raman spectroscopy of carbon-containing particles. *Vibrational Spectroscopy*, 26: 179–186.

Ferrari, A. C. & Robertson, J., 2000. Interpretation of Raman spectra of disordered and amorphous carbon. *Physical Review B*, 61: 14095–14107.

Ferrari, A. C. & Robertson, J., 2001. Resonant Raman spectroscopy of disordered, amorphous, and diamondlike carbon. *Physical Review B*, 64: 075414-1–13.

Freeman, J. J., Wang, A., Kuebler, K. E., Jolliff, B. L. & Haskin, L., A., 2008. Characterization of natural feldspars by Raman spectroscopy for future planetary exploration. *Canadian Mineralogist*, 46: 1477–1500.

Gallegos, J. & Jones, R. H., 2011. Equilibration of feldspar in petrologic type 4–6 L and LL chondrites: metamorphic conditions on chondrite parent bodies. *74th Annual Meeting of the Meteoritical Society, Abstracts*, *University of Greenwich, London, UK, August 8–12, 2011*. The Meteoritical Society, London, p. 5433, A72.

Garde, A. A. & Keulen, N., 2013. Impact melting and mechanical mixing of K-feldspar and plagioclase liquids: Maniitsoq structure, West Greenland. *76th Annual Meteoritical Society Meeting, Abstracts, Edmonton, Canada, July 29 – August 2, 2013*. The Meteoritical Society, Edmonton, p. 5005.

Ghose, S., Choudhury, N., Chaplot, S. L., Pal Chowdhury, C. & Sharma, S. K., 1994. Lattice dynamics and Raman spectroscopy of protoenstatite $Mg_2Si_2O_6$. *Physics of Chemistry and Minerals*, 20: 469–477.

Goldsmith, J. R. & Newton, R. C., 1974. An experimental determination of the alkali feldspar solvus. In: MacKenzie, W. S. &

Zussman, J. (eds), *The Feldspars*. Manchester University Press, Manchester, pp. 337–359.

Goldstein, J. I., Scott, E. R. D. & Chabot, N. L., 2009. Iron meteorites: Crystallization, thermal history parent bodies, and origin. *Chemie der Erde (Geochemistry)*, 69: 293–325.

Hamann, C., Hecht, L., Ebert, M. & Wirth, R., 2013. Chemical projectile–target interaction and liquid immiscibility in impact glass from the Wabar craters, Saudi Arabia. *Geochimica et Cosmochimica Acta*, 121: 291–310.

Hörz, F. Cintala, M. J., See, T. H. & Le, L., 2005. Shock melting of ordinary chondrite powders and implications for asteroidal regoliths. *Meteoritics and Planetary Science*, 40: 1329–1346.

Jones, R. H. & Brearley, A. J., 2011. Exsolution in feldspar in the Tuxtuac (LL5) Chondrite: a new perspective on cooling rates for metamorphosed chondrites. *74th Annual Meeting of the Meteoritical Society, Abstracts, University of Greenwich, London, UK, August 8–12, 2011.* The Meteoritical Society, London, p. 5475, A115.

Karwowski, Ł. & Gurdziel, A., 2009. Secondary minerals in Morasko and Pułtusk meteorites. *Visnyk Lviv University, Series Physics*, 43: 243–248.

Karwowski, Ł., Helios, K., Kryza, R., Muszyński, A. & Drożdżewski, P., 2013. Raman spectra of selected mineral phases of the Morasko iron meteorite. *Journal of Raman Spectroscopy*, 44: 1181–1186.

Karwowski, Ł., Kryza, R., Muszyński, A. & Pilski, A. S., 2012. Outline mineralogy of the Morasko meteorite. In: Muszyński, A., Kryza, R., Karwowski, Ł., Pilski, A. S. & Muszyńska, J. (eds), *Morasko. The Largest Iron Meteorite Shower in Central Europe.* Bogucki Wydawnictwo Naukowe, Poznań, pp. 43–52.

Karwowski, Ł., Kusz, J., Muszyński, A., Kryza, R., Sitarz, M. & Galuskin, E. V., 2015. Moraskoite, Na$_2$Mg(PO$_4$)F, a new mineral from the Morasko IAB-MG iron meteorite (Poland). *Mineralogical Magazine*, 79: 387–398.

Karwowski, Ł. & Muszyński, A., 2006. Silicates Association in nodules of iron meteorites Seeläsgen, Morasko and Jankowo Dolne. *Mineralogia – Special Papers*, 29: 140–143.

Karwowski, Ł. & Muszyński, A., 2008. Multimineral inclusions in the Morasko coarse octahedrite. *Meteoritics & Planetary Science*, 43, 7, A71- A71.

Karwowski, Ł., Muszyński, A., Kryza, R. & Helios, K., 2009. Phosphates in the Morasko meteorite. *Mineralogia – Special Papers*, 35: 90–91.

Kovach, H. A. & Jones, R. H., 2010. Feldspar in type 4–6 ordinary chondrites: Metamorphic processing on the H and LL chondrite parent bodies. *Meteoritics & Planetary Science*, 45: 246–264.

Kracher, A., 1985. The evolution of the partially differentiated planetesimals: Evidence from the iron meteorite groups IAB and IIICD. *Journal of Geophysical Research*, 90 (Suppl.): C689–C698.

Lewis, J. A. & Jones, R. H., 2015. Microtextural study of feldspar in petrologic type 4 ordinary chondrites: contrasting records of parent body metasomatism. *78th Annual Meeting of the Meteoritical Society, Abstracts, University of California, Berkeley, July 27–31, 2015.* The Meteoritical Society, Berkeley, p. 5119.

Lewis, J. A. & Jones, R. H., 2016. Feldspar in the l4 chondrite Saratov: the history and timing of metasomatism. *79th Annual Meeting of the Meteoritical Society, Abstracts, Berlin, Germany, 7–12 August 2016.* The Meteoritical Society, Berlin, p. 6121.

Lewis, J. A., Jones, R. H. & Brearley, A. J., 2016. Alkali feldspar exsolution in ordinary chondrites: alkali metasomatism, meta-

morhpism, and cooling rates. *47th Lunar and Planetary Science Conference, Abstracts, The Woodlands, Texas, March 21–25, 2016.* Lunar and Planetary Institute, National Aeronautics and Space Administration, Woodlands, p. 2559.

MacQueen, J., 1967. Some methods for classification and analysis of multivariate observations. In: LeCam, L.M. & Neymann, J. (eds), *Proceedings of Fifth Berkeley Symposium on Mathematical Statistics and Probability, Volume 1 – Statistics*. University of California Press, Berkeley, California, pp. 281–297.

Matthews, M. J., Pimenta, M. A., Dresselhaus, G., Dresselhaus, M. S. & Endo, M., 1999. Origin of dispersive effects of the Raman D band in carbon materials. *Physical Review B,* 59: R6585.

McCoy, T. J., Keil, K., Scott, E. R. D. & Haack, H., 1993. Genesis of the IIICD iron meteorites: Evidence from silicate-bearing inclusions. *Meteoritics*, 28: 552–560.

McDowell, S. D., 1986. Composition and structural state of coexisting feldspars, Salton Sea geothermal field. *Mineralogical Magazine*, 50: 75–84.

McKenzie, D. & O'Nions, R. K., 1991. Partial melt distributions from inversion of rare earth element concentrations. *Journal of Petrology*, 32: 1021–1091.

McKeown, D. A., 2005. Raman spectroscopy and vibrational analyses of albite: From 25 C through the melting temperature. *American Mineralogist*, 90: 1506–1517.

Mittlefehldt, D. W., Lindstrom, M. M., Bogard, D. D., Garrison, D. H. & Field, S. W., 1996. Acapulco- and Lodran-like achondrites: Petrology, geochemistry, chronology, and origin. *Geochimica et Cosmochimica Acta*, 60: 867–882.

Mittlefehldt, D. W., McCoy, T. J., Goodrich, C. A. & Kracher, A., 1998. Non-chondritic meteorites from asteroidal bodies. In: Papike, J. J. (ed.), *Planetary Materials*, *Reviews in Mineralogy, 36*, pp. 4.1–4.195.

Muszyński, A., Kryza, R., Karwowski, Ł., Pilski, A. S. & Muszyńska, J. (eds), 2012. Morasko. Największy deszcz meteorytów żelaznych w Europie środkowej [Morasko. The largest iron meteorite shower in Central Europe]. *Studia i Prace z Geografii i Geologii, 28.* Bogucki Wydawnictwo Naukowe, Poznań, 111 pp. [In Polish and English.]

Muszyński, A., Stankowski, W., Dzierżanowski, P. & Karwowski, Ł., 2001. New data about the Morasko meteorite. *Mineralogical Society of Poland – Special Papers* 18: 134–137.

Parsons, I., 1978. Alkali feldspars: which solvus? *Physics and Chemistry of Minerals*, 2: 199–213.

Parsons, I. & Lee, M. R., 2009. Mutual replacement reactions in alkali feldspars I: Microtextures and mechanisms. *Contributions to Mineralogy and Petrology*, 157: 641–661.

Parsons, I., Magee, C., Allen, C., Shelley, M. J. & Lee, M. R., 2009. Mutual replacement reactions in alkali feldspars II: Trace element partitioning and geothermometry. *Contributions to Mineralogy and Petrology*, 157: 663–687.

Parsons, I., Fitz Gerald, J. D. & Lee, M. R., 2015. Routine characterization and interpretation of complex alkali feldspar intergrowths. *American Mineralogist*, 100: 1277–1303

Peccerillo, A., Barberio, M. R., Yirgu, G., Ayalew, D., Barbieri, M. & Wu, T. W., 2003. Relationships between mafic and peralkaline silicic magmatism in continental rift settings: a petrological, geochemical and isotopic study of the Gedemsa volcano, Central Ethiopian Rift. *Journal of Petrology*, 44: 2002–2032.

Peccerillo, A., De Astis, G., Faraone, D., Forni, F. & Frezzotti, M. L., 2013. Compositional variations of magmas in the Aeolian arc: implications for petrogenesis and geodynamics. *Geological Society London, Memoirs*, 37: 491–510.

Perugini, D., Petrelli, M. & Poli, G., 2006. Diffusive fractionation of trace elements by chaotic mixing of magmas. *Earth Planetary Science Letters*, 243: 669–680.

Perugini, D. & Poli, G., 2012. The mixing of magmas in plutonic and volcani environments: analogies and differences. *Lithos*, 153: 261–277.

Pilski, A. S., Wasson, J. T., Muszyński, A., Kryza, R. & Karwowski, Ł., 2013. Low-Ir IAB-irons from Morasko and other locations in central Europe: one fall, possibly distinct from IAB-MG. *Meteoritics and Planetary Science*, 41: 1–11.

Pryer, L. L. & Robin, P.-Y. F., 1995. Retrograde metamorphic reactions in deforming granites and the origin of flame perthite. *Journal of Metamorphic Geology*, 14: 645–658.

Pryer, L. L. & Robin, P.-Y. F., 1996. Differential stress control on the growth and orientation of flame perthite: a palaeo-stress-direction indicator. *Journal of Structural Geology*, 18: 1151–1166.

Rapp, R. P. & Watson, E. B., 1995. Dehydratation melting of metabasalt at 8–32 kbar: implications for continental growth and crust–mantle recycling. *Journal of Petrology*, 36: 891–931.

Ruzicka, A., Fowler, G. W., Snyder, G. A., Prinz, M., Papike, J. J. & Taylor, L. A., 1999. Petrogenesis of silicate inclusions in the Weekeroo Station IIE iron meteorite: Differentiation, remelting, and dynamic mixing. *Geochimica et Cosmochimica Acta*, 63: 2123–2143.

Sato, K., Saito, R., Oyama, Y., Jiang, J., Cançado, L. G., Pimenta, M. A. Jorio, A.; Samsonidze, Ge. G. Dresselhaus, G. & Dresselhaus, M. S., 2006. D-band Raman intensity of graphitic materials as a function of laser energy and crystallite size. *Chemical Physics Letters*, 427: 117–121.

Schneider, C. A., Rasband, W. S. & Eliceiri, K. W. 2012. NIH Image to ImageJ: 25 years of image analysis. Nature Methods, 9: 671–675.

Słaby, E., 1992. Changes in the structural state of secondary albite during progressive albitization. *Neues Jahrbuch für Mineralogie, Abhandlungen*, 7: 321–335.

Smith, J. V. & Brown, W. L., 1988. Diffusion, growth, twins and intergrowths (part 4). In: Smith, J. V. & Brown, W. L. (eds), *Feldspar Minerals. 1. Crystal Structures, Physical, Chemical and Microtextural Properties, 2nd edition*. Springer-Verlag, Berlin, pp. 398–647.

Stankowski, W., 2008. Morasko meteorite: a curiosity of the Poznań region. Time and results of the fall. *Adam Mickiewicz University Press, Seria Geologia,* 19: 91.

Stöffler, D., Keil, K. & Scott, E. R. D., 1991. Shock metamorphism of ordinary chondrites, *Geochimica et Cosmochimica Acta*, 55: 3845–3867.

Takeda, H., Bogard, D. D., Mittlefehldt, D. W. & Garrison, D. H., 2000. Mineralogy, petrology, chemistry, and 39Ar–40Ar and exposure ages of the Caddo County IAB iron: evidence for early partial melt segregation of a gabbro area rich in plagioclase–diopside. *Geochimica et Cosmochimica Acta*, 64: 1311–1327.

Tuinstra, F. & Koenig, J. L., 1970, Raman spectrum of graphite. *The Journal of Chemical Physics,* 53: 1126–1130.

Upton, B. G. J., Macdonald, R., Odling, N., Rämö, O. T. & Bagiński, B., 2013. Kűngnât, revisited. A review of five decades of research into an alkaline complex in South Greenland, with new trace-element and Nd isotopic data. *Mineralogical Magazine*, 77: 523–550.

Vance, J. A., 1961. Polysynthetic twinning in plagioclase. *American Mineralogist*, 46: 1097–1119.

Von Stengel, M. O., 1977. Normalschwingungen von Alkalifeldspäten. *Zeitschrift für Kristallografie*, 146: 1–18. [In German, with English abstract.]

Wang, Y., Alsmeyer, D. C. & McCreery R. L., 1990. Raman spectroscopy of carbon materials: structural basis of observed spectra. *Chemistry of Materials*, 2: 557–563.

Wassenburg, G. J., Sanz, H. G. & Bence, A. E., 1968. Potassium-feldspar phenocrysts in the surface of Colomera and iron meteorite. *Science*, 161: 684–687.

Wasson, J. T. & Kallemeyn, G. W., 2002. The IAB iron-meteorite complex: A group, five subgroups, numerous grouplets, closely related, mainly formed by crystal segregation in rapidly cooling melts. *Geochimica et Cosmochimica Acta*, 66: 2445–2473.

Wasson, J. T., Willis, J., Wai, C. M. & Kracher, A., 1980. Origin of iron meteorite groups IAB and IIICD. *Zeitschrift für Naturforschung*, 35a: 781–795.

White, J. C., Parker, D. F. & Ren, M., 2009. The origin of trachyte and pantellerite from Pantelleria, Italy: Insights from major element, trace element, and thermodynamic modelling. *Journal of Volcanology and Geothermal Research*, 179: 33–55.

White, W. M., 2013. *Geochemistry.* Wiley-Blackwell, Hoboken, United States, 668 pp.

Willaime, C. & Brown, W. L., 1974. A coherent elastic model for the determination of the orientation of exsolution boundaries: Application to the feldspars. *Acta Crystallographica*, A30: 313–331.